

# Wideband Millimeter-Wave Propagation Measurements and Channel Models for Future Wireless Communication System Design

Theodore S. Rappaport, *Fellow, IEEE*, George R. MacCartney, Jr., *Student Member, IEEE*,  
Mathew K. Samimi, *Student Member, IEEE*, and Shu Sun, *Student Member, IEEE*

(Invited Paper)

**Abstract**—The relatively unused millimeter-wave (mmWave) spectrum offers excellent opportunities to increase mobile capacity due to the enormous amount of available raw bandwidth. This paper presents experimental measurements and empirically-based propagation channel models for the 28, 38, 60, and 73 GHz mmWave bands, using a wideband sliding correlator channel sounder with steerable directional horn antennas at both the transmitter and receiver from 2011 to 2013. More than 15,000 power delay profiles were measured across the mmWave bands to yield directional and omnidirectional path loss models, temporal and spatial channel models, and outage probabilities. Models presented here offer side-by-side comparisons of propagation characteristics over a wide range of mmWave bands, and the results and models are useful for the research and standardization process of future mmWave systems. Directional and omnidirectional path loss models with respect to a 1 m close-in free space reference distance over a wide range of mmWave frequencies and scenarios using directional antennas in real-world environments are provided herein, and are shown to simplify mmWave path loss models, while allowing researchers to globally compare and standardize path loss parameters for emerging mmWave wireless networks. A new channel impulse response modeling framework, shown to agree with extensive mmWave measurements over several bands, is presented for use in link-layer simulations, using the observed fact that spatial lobes contain multipath energy that arrives at many different propagation time intervals. The results presented here may assist researchers in analyzing and simulating the performance of next-generation mmWave wireless networks that will rely on adaptive antennas and multiple-input and multiple-output (MIMO) antenna systems.

**Index Terms**—Millimeter-wave, path loss, multipath, RMS delay spread, small cell, channel sounder, statistical spatial channel

Manuscript received October 7, 2014; revised March 10, 2015; accepted May 6, 2015. Date of publication May 18, 2015; date of current version September 3, 2015. This material is based upon work supported by the NYU WIRELESS Industrial Affiliates: AT&T, Cable Labs, Ericsson, Huawei, Intel Corporation, InterDigital Inc., Keysight Technologies, L3 Communications, Nokia, National Instruments, Qualcomm Technologies, Samsung Corporation, SiBeam, and Straight Path Communications. This work is also supported by the GAANN Fellowship Program and three National Science Foundation Grants (NSF Accelerating Innovative Research, NetS Medium, and NetS Small). Initial results in this work have been published in [1], [3]–[6], [13], [14], [34]–[36], [38], [39], [44], [62], and [64]. The associate editor coordinating the review of this paper and approving it for publication was M. Juntti.

The authors are with the NYU WIRELESS Research Center, NYU Polytechnic School of Engineering, Brooklyn, NY 11201 USA (e-mail: tsr@nyu.edu; gmac@nyu.edu; mks@nyu.edu; ss7152@nyu.edu).

Color versions of one or more of the figures in this paper are available online at <http://ieeexplore.ieee.org>.

Digital Object Identifier 10.1109/TCOMM.2015.2434384

models, 28 GHz, 38 GHz, 60 GHz, 73 GHz, propagation measurements, MIMO, 5G, SSCM.

## I. INTRODUCTION

THE development and growth of wireless technologies in the past decade has led to the rapid adoption of smartphones and tablets, and emerging wearable devices for health and fitness. Consumers are expecting every device they have to be connected to the network to record, transfer, view, or monitor data. With these new technologies comes the demand for more data, video, and content access. While the growth in wireless devices and technologies has sky-rocketed, the spectrum available for these devices has not kept pace. Carriers and other fixed or mobile service providers are reaching the upper bounds of channel capacity, and the reality of a spectrum shortfall is now becoming increasingly clear. The wireless spectrum below 6 GHz will not be enough to meet future needs, as the current global allocation of cellular and unlicensed wireless local area network (WLAN) spectrum is quite small when compared to the vast spectrum available between 6 and 300 GHz [1]–[4]. In the past 40 years since the advent of the modern mobile communications industry, clock speeds and memory sizes of communications and computer devices have increased by 4 to 6 orders of magnitude (or more), while the carrier frequencies of all WLAN and cellular networks have increased by less than an order of magnitude, from 450 MHz first generation cellphones, to today's 2 GHz 4G/LTE systems [2], [3], [5]–[7].

The demand for content will continue growing at extreme rates, such that annual mobile traffic will exceed 291.8 Exabytes (EBs) by 2019 [7], [8]. CISCO has forecasted that mobile data traffic will increase from 2.5 EBs per month in 2014 to 24.3 EBs per month in 2019 [7]–[9]. Existing allocated spectrum will not provide enough bandwidth for carriers to increase capacity for meeting the growing demand, even with smaller cells, heterogeneous networks, complex modulation schemes and MIMO systems. By the year 2020, Nokia and Samsung predict a 10,000x increase in traffic on wireless networks with virtually no latency for content access [6], [10]. With the massive impending traffic growth and a global spectrum shortfall below 6 GHz, there are only a few potential avenues that will satisfy the pending capacity explosion.

Utilizing unused raw mmWave spectrum is one key enabling solution for meeting the extreme data demand growth.\* While mmWave spectrum offers a great opportunity to increase capacity, little is known about the channel propagation characteristics for mobile access networks in dense urban environments at these carrier frequencies. In the past, mmWave spectrum was primarily used for satellite communications, long-range point-to-point communications, military applications, and Local Multipoint Distribution Service (LMDS) [11], [12]. MmWave frequencies have much smaller wavelengths, ranging from 1 mm to 10 mm, about the size of a human fingernail, whereas 4G frequencies have wavelengths that are tens of centimeters. Smaller wavelengths at mmWave frequencies have often been thought to result in higher attenuation (due to oxygen absorption and precipitation) through air, than that observed at today's cellular bands. It is true that mmWave frequencies undergo greater free space attenuation in the first meter of propagation once leaving an antenna, than today's Ultra High Frequency (UHF) cellular frequencies; however, atmospheric attenuation across most of the mmWave spectrum only induces a fraction of a dB to just a few dB of additional loss at a 1 km distance, compared to UHF bands [1], [4]. Only at certain frequency bands, such as 60, 180, or 380 GHz, do molecular resonances create high atmospheric attenuation causing signals to attenuate much more rapidly with distance than today's UHF/microwave bands. These specific high attenuation mmWave bands will be better suited for local or personal area communications, or "whisper radios" with coverage distances of a few meters (m) [1]–[3]. Rain attenuation only contributes a few dB of additional propagation path loss at mmWaves compared to free space when considering inter-site base station distances of no more than a few hundred meters, implying that the impact of rain will be mollified through the use of high gain, steerable antennas [3], [13], [14].

In late 2014, the Federal Communications Commission (FCC) put forth a notice of inquiry (NOI) in FCC 14-154 and FCC 14-177, to gain a better understanding of the spectrum bands above 24 GHz for mobile radio services [15], [16]. The NOI asked more than 170 questions regarding technology specifications, bandwidth allocations, health effects, and more, in order to gain insight into the viability of mmWave bands for future mobile wireless communications. Numerous corporations and academic institutions, including the NYU WIRELESS research center and many of its industrial affiliate sponsors, responded to these questions to educate the FCC about industrial and academic studies already conducted at mmWave bands, to motivate them to open up this spectrum. In early 2015, UK's Ofcom sought similar public comments [17].

Aside from work conducted by authors at the University of Texas at Austin (UTA) and New York University (NYU), there have been relatively few published propagation studies at mmWave bands in dense urban environments for mobile access and backhaul communications. Many propagation studies performed at mmWave bands for these types of applications considered line-of-sight (LOS), point-to-point, or indoor test scenarios. Kyrö *et al.* at Aalto University performed channel

measurements in the E-band from 81–86 GHz over 5 GHz of bandwidth for point-to-point communications in a long street canyon environment in Helsinki, Finland [18]. Measurements determined the channel's average root-mean-square (RMS) delay spread due to multipath scattering in the canyon environment, and compared the measurements with simulated RMS delay spreads. The results showed very little multipath delay spread, and yielded excellent agreement between measured and modeled (stochastic based geometrical single-bounce model [19]–[21]) delay spreads [18]. The difference between mean values was only 0.027 ns, where the maximum modeled RMS delay spread was only 0.25 ns [18]. Kyrö *et al.* also performed channel impulse response measurements by frequency sweeping across the 81–86 GHz band for both a street canyon and roof-to-street scenario [22]. Similar to [18], only a few LOS measurements were performed to prove that the LOS component was dominant in the channel when using highly directional antennas [22]. The study proved that multipath exists in the E-band channel, but extensive channel measurements for mobile or backhaul were not reported.

Many studies for the 28 GHz LMDS band were conducted to assess coverage, large-scale path loss, and fading and multipath effects. Measurements by Elrefaie *et al.* showed that better coverage was obtained for higher transmitter (TX) antenna heights than for lower heights [23], due to less obstructions. Violette *et al.* performed wideband non-line-of-sight (NLOS) studies in the 9.6, 28.8, and 57.6 GHz bands in downtown Denver, and measurements showed significant signal attenuation (as great as 100 dB) due to large building obstructions [24]. Penetration tests for glass with metalized layers showed that attenuation increased by 25 to 50 dB per layer [24], [92]. The results also revealed that delay spreads were no more than 10 ns relative to the LOS component when transmitting over 500 MHz of bandwidth while using narrowbeam, linearly polarized antennas. Foliage attenuation measurements at the 35 GHz band resulted in a mean attenuation of 24.8 dB through approximately 15 m of red pine trees, and revealed a considerable loss in excess of free space [25]. Propagation through a canopy of orchard trees was tested using CW signals at 9.6, 28.8, and 57.6 GHz which indicated that through the first 30 m of foliage depth, signal attenuation over distance is linear with approximately 1.3–2.0 dB/m of loss, and beyond this distance attenuation was only about 0.05 dB/m, revealing that scattering dominates propagation deep into foliage [26], [91].

The 60 GHz band has been one of the most studied mmWave bands as it is currently used for unlicensed WirelessHD and Wireless Gigabit Alliance (WiGig) WLAN devices [1], [27], that offer multiple gigabits per second data rates for short range indoor communications. A majority of measurements were conducted for indoor applications due to the earliest intended use cases (WLAN), and high oxygen absorption centered around 60 GHz [3]. However, with the 2013 FCC part 15 rule change that greatly expanded the effective radiated power of WLAN devices in the 60 GHz band from 40 to 82 dBm [1], 60 GHz outdoor communication for unlicensed backhaul applications has just recently garnered great interest. Outdoor studies at 59 GHz were conducted in Oslo city streets, and showed that a majority of delay spreads were less than 20 ns over 7 different street

\*Frequencies from 30 GHz to 300 GHz are commonly known as mmWave frequencies, although industry often uses the term mmWave to define frequencies between 10 and 300 GHz [1].

scenarios for LOS and obstructed environments [28]. Wideband measurements with 200 MHz of bandwidth revealed that city streets do not cause much multipath, as the RMS delay spread was observed to be lower than 20 ns [29]. Measurements and models showed that path loss in LOS environments behaves almost identical to free space, with a *path loss exponent* (PLE) of 2 (i.e., power decays as the square of the distance). In regards to path loss between 1.7 GHz and 60 GHz, Smulders *et al.* showed that the most significant difference in path loss between these frequency bands is the initial close-in free space path loss induced by the increase in carrier frequency due to Friis' free space equation [29], [30]. Other outdoor measurements in a city street environment at 55 GHz showed that power decreased much more rapidly with distance through narrower streets compared to a direct path or through wide city streets [31], and the coherence bandwidth range of 20–150 MHz closely matched the results by Violette *et al.* in [24]. Additionally, recent outdoor studies at 60 GHz in a street canyon environment indicated that the LOS path is most dominant but that the ground reflected path is significant at larger distances where the LOS path may be blocked, resulting in an overall PLE of 2.13, very close to theoretical free space (PLE = 2) [32].

Samsung has been active in measuring mmWave channels for future mobile communications. Initial tests were performed at 28 GHz and 40 GHz to study penetration losses for common obstructions such as wood, water, hands, and leaves [33], [92]. Results showed that metal and water can attenuate the signal by 30 to 40 dB when very close to the receiver (RX); however, when moved further away, more reflected energy of the signal was able to reach the RX with relatively widebeam antennas. For LOS outdoor measurements at 28 GHz, a PLE of 1.98 (virtually identical to the theoretical free space value of 2) was measured for distances up to 100 m [33]. Increased signal strength was also reported at the RX in LOS environments when the RX elevation was uptilted and downtilted, attributed to captured reflected energy from both the ground and surrounding buildings. In NLOS environments in Austin, Texas, we observed from angle of arrival (AOA) measurements that wider beamwidth antennas captured more received power than higher gain, narrower beamwidth antennas, as reported in [34]–[36].

Samsung Electronics announced in May of 2013 that they were able to transmit data up to 1.056 Gbps at 28 GHz over distances up to 2 km using an adaptive array transceiver with multiple antenna elements [37]. While this early work did not include extensive measurements, Samsung is currently using a channel sounder that measures power delay profiles (PDPs) from multiple directions of arrival to create omnidirectional-like wideband channel measurements, while benefiting from high-gain antennas (based on approaches in [38]–[41]), to provide statistics necessary to build channel models similar to WINNER II and 3GPP for the 28 GHz wideband urban channel [42], [43]. Work at NYU WIRELESS described here has also focused on providing 3GPP-like channel models, including omnidirectional path loss models synthesized from directional channel measurements, and statistical 3-D channel impulse response models for directional and omnidirectional systems for use in emerging mmWave standard bodies [1], [3], [13], [38], [39], [41], [44]–[49].

The vast body of previous published work used for earlier versions of wireless technologies provides valuable insight into best practices for measuring and modeling directional mmWave wideband channels. Researchers have already studied directional UHF CDMA cellular radio systems [50]–[52]. Work in [52] showed that with correlated multipath, adaptive antenna arrays with just a few elements provided larger improvements in performance than a switched beam system. In addition to measurements, ray-tracing methods provided accurate predictions of wireless communication channel properties, such as path loss and RMS delay spreads, and may be used as a substitute for propagation measurements which are time-consuming and expensive. Further, ray-tracing is widely used to help with site-specific deployments [1]. 3-D ray-launching uses geodesic spheres and distributed wavefronts to simulate electromagnetic propagation, offering a simple and accurate propagation prediction method with low computational complexity [53].

Once accurate statistical models are developed for mmWave frequencies (often with the assistance of ray-tracing to fill in missing or sparse data), simulations for performance, capacity, and availability can be carried out to evaluate air-interface trade-offs. Previous work showed that with the use of real-time DSP techniques and adaptive antenna arrays, capacity and signal-to-noise ratio (SNR) improvements could be made for systems at UHF bands [54], [55]. Similar simulations are necessary for mmWave wireless systems; however, at these higher frequencies with new adaptive antenna architectures, there will be trade-offs on how and where processing will take place [1], [49], [56]. More reliance on analog processing at either or both the RF (Radio Frequency) or IF (Intermediate Frequency) may be possible as technological advancements are made [1], [3], [6], [43], [56]–[60].

Extensive mmWave channel propagation measurements with thousands of recorded PDPs over a wide range of urban microcell (abbreviated as UMi in the 3GPP standard) and urban macrocell (UMa) [50] environments have been conducted at UTA and NYU [3], [13], [14], [34]–[36], [39], [44], [57], [61]–[65]. These measurements and resulting channel models will aid researchers in the evaluation and design of future 5G mmWave systems. This paper serves as a detailed compilation of all mmWave measurements made by the authors from 2011 through 2013 with the benefit of more stringent data processing, experience, feedback, and requirements received from industry and academia over the past few years.

When writing this invited paper, we realized, in hindsight, that researchers in the channel modeling or propagation measurement fields often do not standardize or even define decisions made in their measurement or modeling approach, or their thresholding approach, yet such standardization yields much more meaningful and useful results between different researchers, allowing for easy comparisons and improvements. Thus, in this paper, we cast all of our previous work in a single, referenceable, standard approach for path loss (by referencing all received powers to a 1 m close-in free space reference distance), and elucidate practices that will allow the community to compare propagation and channel results in a more unified manner. For example, we provide a standard noise threshold for multipath PDP thresholding (using a 5 dB SNR threshold).

Section II describes the customized hardware used to perform the mmWave channel measurements and describes the measurement locations and operating scenarios in the UMi environment for each of the four bands of 28, 38, 60 and 73 GHz, in addition to UMa measurements (TX heights of 23 m and 36 m) at 38 GHz. Sections III and IV provide measured directional and omnidirectional path loss models, based on thousands of wideband PDPs measured in various scenarios (outdoor mobile access and outdoor backhaul). Section V shows the value of a simple  $d_0 = 1$  m path loss model for comparing the distance extension available through beam combining [41]. Section VI presents measured mmWave outage studies, using randomly placed transmitters and receivers in UMi environments. Section VII presents the measured multipath and RMS delay spread characteristics of mmWave channels when using steerable antennas, for cases with arbitrary antenna steering, and also when directionally steering the antenna to the strongest arriving signal. Section VIII provides spatial statistics of mmWave channels, for the purpose of extending UHF/Microwave industry standard channel models to properly reflect the observed phenomena in mmWave channels, and we introduce a new channel modeling concept, the *spatial lobe*, that characterizes mmWave outdoor urban channels. Section IX presents characterizations of outdoor peer-to-peer (or device-to-device) channels and propagation into vehicles, and Section X introduces a wideband statistical spatial channel impulse response model based on NLOS measured data at 28 GHz and 73 GHz in New York City. Conclusions are drawn in Section XI.

## II. WIDEBAND mmWAVE MEASUREMENT DESCRIPTIONS AND HARDWARE SPECIFICATIONS

Wideband propagation studies at 28, 38, 60, and 73 GHz using first null-to-null RF channel sounding bandwidths of 800 MHz and 1.5 GHz were conducted in 2011 in Austin, and in 2012–2013 in New York City, to explore a wide range of mobile use cases over many transmitter-receiver (T-R) separation distances, in order to create 5G mmWave channel models. The four frequency bands were chosen for testing due to the likelihood of eventual use of this spectrum for ultrawideband mobile radio applications (indeed, [16] and [17] have recently suggested these bands will likely become available for mobile use) at these carrier frequencies. The 28 and 38 GHz bands were licensed for LMDS and backhaul communications, but the technology was not ready for market in the 1990's [11], [34]. The 60 GHz band experiences excessive attenuation due to oxygen absorption compared to other bands, but as explained in the Introduction, is a viable and attractive option for short-range (a few hundred meters) point-to-point (backhaul) applications as well as indoor Wi-Fi [27], [66]. 73 GHz is centered in 71–76 GHz E-band which is presently lightly-licensed globally, and relatively unexplored for mobile communications [10].

### A. Hardware Descriptions and Specifications

Each measurement campaign used a common spread spectrum sliding correlator design with a double conversion super-heterodyne RF architecture at the TX and RX, and common

baseband/IF components. The common architecture consisted of the baseband signal upconverted to an IF between 5 and 7 GHz, and then mixed with a local oscillator up to the corresponding RF frequency for each campaign, where a pyramidal horn antenna was connected to the RF waveguide output. The received signal was then captured by a rotatable pyramidal horn antenna connected to a waveguide flange input at the RX where the signal was mixed with a local oscillator to obtain an IF between 5 and 7 GHz, and was then downconverted back to baseband. Pyramidal horn antennas that could be steered with relatively high gain ( $> 13$  dBi) were used to collect channel data representative of future mmWave mobile devices that will employ beam steering antennas. Detailed specifications for the hardware used for each campaign is displayed in Table I.

### B. Sliding Correlator Channel Sounder Theory and Design

A spread spectrum sliding correlator channel sounding method was used for each of the four measurement campaigns conducted in the mmWave spectrum (i.e. 28, 38, 60, and 73 GHz) [30], [67]–[69]. The fundamental concept of sliding correlation uses the correlation properties of two identical pseudorandom noise (PN) sequences at slightly different clock speeds generated at the TX and RX, resulting in a time dilated (bandwidth compressed) signal with processing gain that greatly improves SNR [70]. This technique allows for a narrowband detector while using a wideband PN sequence, while simultaneously providing additional link margin arising from the benefit of processing gain, so long as the channel remains pseudo-static during the averaging period where the two PN sequences slide past each other over a complete cycle [30], [67]–[70]. In mmWave communications, modulation symbols will have durations on the order of nanoseconds due to the much greater channel bandwidths, hence a wideband sliding correlator channel sounder offers an effective way to achieve excellent ns-scale temporal resolution and good dynamic range of the measured PDP [1], [59].

Our sliding correlator channel sounder produced a digital PN sequence using custom printed circuit boards that housed emitter-coupled-logic (ECL) shift registers to produce an 11-bit maximal length code with the shift registers tapped at the 9<sup>th</sup> and 11<sup>th</sup> flip-flop outputs [61]. Different frequency bands were measured by changing local oscillator frequencies, IF frequencies, and the RF front-ends; specifications and detailed block diagrams are given in [3], [13], [34], [61], [63], [65].

The transmitted pseudorandom binary sequence (PRBS) for the 28 GHz and 73 GHz campaigns had an 800 MHz RF spread spectrum first null bandwidth (we used a square-wave, non-shaped 400 Mcps baseband PN sequence). After propagating through the radio channel and upon reaching the RX antenna (rotatable horn antenna), the received wideband signal was downconverted to IF, where it was bandpass filtered, attenuated (for maintenance of proper linear range and maximum display range on the baseband digitizing oscilloscope detector) and amplified with a low-noise amplifier. After amplification, the IF signal was demodulated into its in-phase ( $I$ ) and quadrature ( $Q$ ) baseband signal components [61]. Both the  $I$  and  $Q$  signals were then correlated with a reference PN sequence that is identical to the transmitted sequence but clocked at a slightly slower rate, in order to create a time dilated cross-correlation. For example,

TABLE I  
HARDWARE SPECIFICATIONS OF THE 28, 38, 60, AND 73 GHz MEASUREMENTS

Campaign	28 GHz (2012)	38 GHz (2011)	60 GHz (2011)	73 GHz (2013)
Center Frequency	28 GHz	37.625 GHz	59.4 GHz	73.5 GHz
Antenna Sweeps	Yes	No	No	Yes
Broadcast Sequence	11 <sup>th</sup> order PN Code ( $L = 2047$ )			
TX and RX Antenna Type	Rotatable Pyramidal Horn Antenna			
TX Chip Rate	400 Mcps		750 Mcps	400 Mcps
RX Chip Rate	399.95 Mcps		749.9625 Mcps	399.95 Mcps
Slide Factor $\gamma$	8000		20000	8000
TX Ant. Gain	24.5 dBi; 15 dBi	25 dBi		27 dBi
TX AZ Ant. HPBW	10.9°; 28.8°	7.8°	7.3°	7°
TX EL Ant. HPBW	8.6°; 30°	7.8°	7.3°	7°
RX Ant. Gain	24.5 dBi; 15 dBi	25 dBi; 13.3 dBi	25 dBi	27 dBi
RX AZ Ant. HPBW	10.9°; 28.8°	7.8°; 49.4°	7.3°	7°
RX EL Ant. HPBW	8.6°; 30°	7.8°; 49.4°	7.3°	7°
Antenna Polarization (TX-to-RX)	V-V, V-H, H-V, H-H	V-V		
Max Transmit Power	30.1 dBm	21.2 dBm	5 dBm	14.6 dBm
Max EIRP	54.6 dBm	46.2 dBm	30 dBm	41.6 dBm
Max Measurable Path Loss	178 dB	150 - 160 dB <sup>†</sup>	150 dB	181 dB

<sup>†</sup>160 dB was used for outage study signal detection, where a signal was detectable with the measurement equipment, but accurate PDPs could not be recorded as the signal was very close to the noise floor.

during the 73 GHz campaign, the TX code (PN code length 2047) was transmitted at 400 Mcps and the RX code was set to 399.95 Mcps, allowing for a time dilation factor, or slide factor  $\gamma$ , calculated to be 8 000 as follows:

$$\gamma = \frac{f_{TX}}{f_{TX} - f_{RX}} = \frac{400 \text{ MHz}}{400 \text{ MHz} - 399.95 \text{ MHz}} = 8,000 \quad (1)$$

The PN sequence duration (the period  $T$ ) of the transmitted sequence is a function of the chip rate and length of the sequence:  $T = \frac{1}{400 \text{ MHz}} \times 2047 = 5.11 \mu\text{s}$  and the chip duration is  $t_0 = \frac{1}{400 \text{ MHz}} = 2.5 \text{ ns}$ . Therefore, after a time-dilated cross-correlation with slide factor  $\gamma$  of 8,000, the period between successive cross-correlation peaks is:  $2.5 \text{ ns} \times 8,000 \times 2047 = 40.94 \text{ ms}$  for the raw acquisition of one PDP. A National Instruments USB-5133 digitizer sampled the time-dilated  $I$  and  $Q$  cross-correlated voltages, and the corresponding received power was recovered using National Instruments LabVIEW software, programmed to square and add the two voltage components  $I^2 + Q^2$ , thereby recovering a raw PDP. Twenty successive raw PDPs were averaged for each PDP acquisition ( $40.94 \text{ ms} \times 20 = 818.8 \text{ ms}$  for each recorded PDP) in order to increase the SNR and eliminate abrupt dynamic changes during the acquisition interval. The absolute axis of the time-dilated PDP was recovered by dividing the measured (dilated) PDP time scale by the slide factor  $\gamma$ . The slide factor is related to the RF bandwidth that can be measured compared to the baseband bandwidth needed for reception [30]. In our case, the baseband bandwidth for reception was 50 kHz (PN clock rate divided by the slide factor: in this case for a 400 Mcps sequence and a slide factor of 8 000). The use of highly-directional steerable horn antennas at the TX and RX provided the ability to capture directional azimuth and elevation plane measurements over the complete azimuth plane and many elevation angles, and provided a large link margin and system dynamic range as compared to what is achievable with low-gain omnidirectional

antennas. From the PDPs measured at distinct azimuth and elevation angles, multipath channel parameters were extracted through post-processing techniques, and directional and omnidirectional channel models were formed [38], [41], [45], [65].

### C. Channel Sounding Triggering and Thresholding

Typical channel sounding systems track the absolute or relative time of arrival of a propagating signal in order to determine precise temporal characteristics of a wireless channel. A popular channel sounding technique uses a Vector Network Analyzer (VNA) to measure the gain of the S21 parameter of the wireless channel, discretely across a wide range of frequencies (frequency swept sounding). In such a system, the TX and RX are physically connected to the VNA through a phasing cable, for knowledge of the precise phase at each discrete tone. Since the VNA measurement system consists of both the source and sink, accurate timing information is possible since the transmitted probing signal and acquisition recording are generally triggered via the same mechanism. Since the VNA is a one-box cable-connected system, it is not usually used to measure large T-R separation distances [30]. Also, the channel must be assumed static during the wideband frequency sweep (sometimes more than many seconds per measurement). For these reasons, VNAs are generally relegated to indoor channel sounding [30].

Time domain channel sounding systems, such as the sliding correlator, obtain timing information by either using exact timing at both the TX and RX from rubidium, cesium, or global positioning system (GPS) timing sources, or by using relative timing information, where the RX triggers on the first arriving multipath component (MPC) [1], [30]. Our channel sounder relied upon relative timing information via a triggering algorithm that logged free running data and time-aligned successive oscilloscope captures on the signal peak in a PDP window. The lack of an absolute timing reference required us to use ray-tracing

to synthesize the exact propagation times of channel impulse responses received from different antenna pointing angles, so that the statistical channel models given in Section X would accurately account for temporal characteristics over space. In general, the LOS component is the strongest (first arriving) peak at the RX, and for reasonable SNR (greater than 5 dB), NLOS signals have stable first arriving signal levels, even if they are weaker than stronger, later-arriving MPCs. Temporal channel statistics such as relative excess delay and RMS delay spread do not require synchronized timing [30].

Once the raw PDPs were recorded they were thresholded based on a 5 dB SNR threshold relative to the mean thermal noise floor of the raw PDP, allowing us to keep a consistent noise floor threshold across all measurements, rather than other approaches reported in the literature [71] that use a threshold relative to the maximum multipath peak. The 5 dB SNR threshold was found for each measurement by computing the average noise power of the last several hundred ns of each PDP that had no detectable multipath, and we used the mean value of the noise in order to apply the 5 dB SNR threshold for detecting (and keeping) all MPCs in that PDP. Since all PDPs were measured using an RX gain that was manually adjusted to provide a large dynamic range on the received baseband PDP, an absolute SNR threshold does not artificially limit the sensitivity of the measured data and allows users to properly mimic actual wideband receiver functionality that will be implemented with automatic gain control (AGC) in future wideband mmWave mobile devices. This stringent 5 dB SNR thresholding was developed and applied to the measured data after initial measurements in [3] were published, thus RMS delay spreads and excess delays reported in [3] are larger than those presented here, since the earlier processed measurements included noise that has been subsequently removed (e.g., not considered to be multipath) using the more stringent 5 dB SNR thresholding technique. Thus, the noise thresholding of measured channel impulse responses is critical when interpreting PDP channel time dispersion results. For this reason, we advocate that all channel modeling activities specify a particular SNR thresholding as described above, since it is a practical thresholding level for wideband low-cost radios that are either non-coherent or that have typical noise figure or high phase noise [1], and allows repeatability by others without relying on particular measurement peaks that are widely variable for different pointing angles, locations, or measurement systems.

#### D. Measurement Descriptions and Methodologies

The measurement campaigns for each frequency band included numerous wideband multipath PDP large-scale path loss measurements for multiple AOA and Angle of Departure (AOD) orientations between the TX and RX, using various TX heights and deployment scenarios. Each propagation measurement campaign used mechanically steerable directional horn antennas, where the AOD for the transmitted signal was determined by the orientation of the TX antenna. Each individual wideband channel PDP measurement of every campaign was recorded for a specific TX and RX (TX-RX) location at specific directional antenna azimuth and elevation pointing angles between the TX and RX. This resulted in thousands of acquired PDPs, each one being a function of TX location  $i$ , TX height

$h_{TX}$  in meters, RX location  $j$ , RX height  $h_{RX}$  in meters, TX antenna gain  $G_{TX}$  in dBi, TX antenna azimuth and elevation angles  $\theta_t$  and  $\phi_t$  in degrees, respectively, RX antenna gain  $G_{RX}$  in dBi, RX antenna azimuth and elevation angles  $\theta_r$  and  $\phi_r$  in degrees, respectively, and 3-D T-R separation distance  $d$  in units of meters.

The 28 and 73 GHz campaigns consisted of *systematic antenna sweeps* that recorded PDPs at incremental angles across the entire azimuth plane for several TX and/or RX fixed elevation angles, whereas the 38 GHz and 60 GHz measurements randomly searched for signal at various angles in the azimuth and elevation planes, and only those PDPs with distinguishable energy were recorded. Sweeps in the azimuth plane at various fixed elevation planes allowed us to collect realistic channel impulse response measurements for future mmWave mobile devices that will take advantage of directional beam steering antennas and algorithms. Descriptions and specifications for each measurement campaign in each mmWave band are now presented.

1) *28 GHz Measurement Descriptions*: 28 GHz propagation studies were conducted in 2012 in downtown Manhattan around NYU's main campus, along with a smaller study conducted in downtown Brooklyn around the NYU Polytechnic School of Engineering campus, with a maximum RF transmit power of 30.1 dBm over an 800 MHz first null-to-null RF bandwidth, yielding a maximum measurable dynamic range of 178 dB. In both studies, measurements were performed for a typical base station-to-mobile (access) scenario with the TX antenna on relatively low rooftops and the RX antenna located at a mobile height (1.5 m) around common city blocks typical of a dense urban environment. The majority of measurements were conducted using narrowbeam TX and RX antennas, each with 24.5 dBi gain and 10.9° half-power beamwidth (HPBW) in the azimuth (Az.) plane in both Manhattan and Brooklyn. As shown in Table I, elevation (El.) HPBW is comparable to azimuth (Az.) HPBW. A small subset of measurements in Manhattan were conducted with a wider 28.8° HPBW 15 dBi gain antenna at the RX for five locations, and an additional measurement from an outdoor TX to an indoor RX was recorded, but the dataset is too sparse to present here. Another small subset of measurements were conducted in Brooklyn with a wider 28.8° HPBW antenna at the TX, for four RX locations (using 10.9° HPBW antennas), in addition to a small number of cross-polarized antenna measurements [3], [62], [72]. Both sets of Brooklyn measurements included automated small-scale track measurements at two locations, in order to study small-scale spatial correlation of fading at mmWave frequencies [62]. The narrowbeam outdoor-to-outdoor measurements in Manhattan consisted of over 10,000 recorded PDPs using three TX locations and 27 RX locations that were visited repeatedly for each TX location, providing for a total of 74<sup>‡</sup> TX-RX location combinations. For each TX-RX location combination, the RX antenna was swept in 10° increments (approximately the antenna HPBW) in the azimuth plane for three different RX antenna elevation pointing angles and three different TX

<sup>‡</sup>Not all 27 RX locations were measured for each of the three TX locations due to time, student, and equipment availability.

TABLE II  
T-R SEPARATION DISTANCES FOR SPECIFIC TX LOCATIONS AT 28 GHz IN MANHATTAN AND BROOKLYN WHERE SIGNAL WAS RECORDED.  
LOS ENVIRONMENTS ARE WHEN THE TX AND RX LOCATIONS HAD A CLEAR OPTICAL PATH TO ONE ANOTHER.  
NLOS ENVIRONMENTS CONTAIN OBSTRUCTIONS BETWEEN THE TX AND RX

<b>28 GHz Manhattan Measurements (RX: 1.5 m) (TX/RX Antenna Az. HPBW: 10.9°)</b>		
<b>TX Location (Abbr.) [height]</b>	<b>Environment</b>	<b># of Locations with Signal</b>
Coles Sports Center 1 (COL1) [7 m]	LOS	2 (31 m $\leq d \leq$ 102 m)
	NLOS	6 (61 m $\leq d \leq$ 162 m)
Coles Sports Center 2 (COL2) [7 m]	LOS	1 ( $d =$ 51 m)
	NLOS	7 (74 m $\leq d \leq$ 169 m)
Kaufman (KAU) [17 m]	LOS	3 (33 m $\leq d \leq$ 54 m)
	NLOS	7 (77 m $\leq d \leq$ 187 m)
<b>28 GHz Brooklyn Measurements (RX: 1.5 m) (TX/RX Antenna Az. HPBW: 10.9°)</b>		
Rogers Hall (ROG1) [40 m]	NLOS	5 (110 m $\leq d \leq$ 135 m)
<b>28 GHz Brooklyn Measurements (RX: 1.5 m) (TX/RX Antenna Az. HPBW: 28.8°/10.9°)</b>		
Rogers Hall (ROG1) [40 m]	NLOS	4 (110 m $\leq d \leq$ 135 m)

azimuth angles, all with a fixed TX downtilt elevation of  $-10^\circ$ , where a PDP was acquired at each distinct azimuth pointing increment at the RX. One TX antenna sweep was conducted as well, resulting in 10 total azimuth sweeps for each TX-RX combination. This approach allowed us to measure the vast majority of received multipath power over 3-D, without wasting time to exhaustively measure every possible spherical pointing direction at the TX and RX. By having a sufficient number of PDPs that substantially represented all of the possible measured power at each location, omnidirectional channel models were created, as described in Section IV. T-R separation distances ranged from 31 m to 425 m, but PDPs were not measurable beyond 200 m. Table II shows a description of TX sites and separation distances for LOS and NLOS environments where signal was recorded for corresponding TX sites, while site layouts and detailed descriptions of the measurement procedures are given in [3], [62], [73]. For the remainder of this article, 28 GHz *narrowbeam* measurements will refer to those conducted in Manhattan with steerable antennas having HPBW of  $10.9^\circ$  at both the TX and RX, whereas *widebeam* measurements will refer to measurements conducted in Brooklyn using a steerable  $28.8^\circ$  HPBW antenna at the TX and a  $10.9^\circ$  HPBW antenna at the RX.

### 2) 38 GHz Measurement Descriptions:

*a) Base Station-to-Mobile Access Scenario:* 38 GHz cellular measurements were conducted with four TX locations chosen on buildings at the UTA campus in the summer of 2011, with a maximum RF transmit power of 21.2 dBm over an 800 MHz first null-to-null RF bandwidth and a maximum measurable dynamic range of 160 dB, for RX locations in the surrounding campus using narrowbeam TX antennas ( $7.8^\circ$  Az. HPBW) and narrowbeam ( $7.8^\circ$  Az. HPBW) or widebeam ( $49.4^\circ$  Az. HPBW) RX antennas. A total of 43 TX-RX location combinations were measured for narrowbeam measurements (with T-R separation distances ranging from 29 m to 930 m) and 22 TX-RX location combinations were measured for widebeam measurements (with T-R separation distances between 29 m and 728 m), as given in [36]. Fig. 2 in [35] presents a map of the measurement locations of the 38 GHz campaign, where for each TX-RX location combination, PDPs for several TX and RX antenna azimuth and elevation pointing angle combinations

were recorded. Table I provides hardware specifications for the 38 GHz measurements. For the remainder of this article, 38 GHz *narrowbeam* measurements will refer to a 25 dBi gain antenna with  $7.8^\circ$  HPBW at both the TX and RX, whereas *widebeam* measurements will refer to a 13.3 dBi gain antenna with  $49.4^\circ$  HPBW at the RX and a  $7.8^\circ$  HPBW antenna at the TX.

*b) Peer-to-Peer Scenario:* Peer-to-Peer (P2P, also called device-to-device (D2D)) measurements were made using identical 38 GHz Ka-Band vertically polarized antennas with gains of 25 dBi ( $7.8^\circ$  Az. HPBW) at the TX and RX. A single TX and ten random RX locations with T-R separation distances ranging from 19 m to 129 m were selected around a pedestrian walkway area surrounded by many buildings on the UTA campus. Several PDPs for both LOS and NLOS scenarios were recorded. The directional antennas were also rotated in the azimuth plane, but in a systematic way to search for large scatterers from all possible azimuthal directions [34]. A map of the P2P measurement locations is displayed in Fig. 1 in [34].

### 3) 60 GHz Measurement Descriptions:

*a) Peer-to-Peer Scenario:* 60 GHz P2P measurements were similar to those recorded at 38 GHz, including the same single TX and ten random RX locations, with a maximum RF transmit power of 5 dBm over 1.5 GHz first null-to-null RF bandwidth and a maximum measurable dynamic range of 150 dB. Similar to the 38 GHz measurements, a set of 25 dBi gain horn antennas ( $7.3^\circ$  Az. HPBW) were used at the TX and RX. See [61] and [34] for detailed descriptions of the 60 GHz P2P measurement layout and specifications.

*b) Vehicular Scenario:* The 60 GHz vehicular propagation measurements were aimed at investigating car-to-signpost and car-to-car communications at mmWave frequencies. Measurements were conducted in a parking lot on the UTA campus in 2011. The RX antenna was placed at head level of a seated passenger, inside a standard-sized sedan automobile, and the 1.5 m high TX antenna was placed 4 m, 12 m, and 23 m away from the car with horn antennas having 25 dBi of gain directed from the TX to the vehicle. The T-R separation distances represented distances corresponding to a single lane of traffic, a two-way street, and a multi-lane highway, respectively [74]. Measurements were taken at two RX sites within the vehicle: the driver position and a rear passenger position, as shown in

TABLE III  
T-R SEPARATION DISTANCES FOR SPECIFIC TX LOCATIONS AT 73 GHz IN MANHATTAN WHERE SIGNAL WAS RECORDED AT THE RX FOR ACCESS AND BACKHAUL MEASUREMENTS. LOS ENVIRONMENTS ARE WHEN THE TX AND RX LOCATIONS HAD A CLEAR OPTICAL PATH TO ONE ANOTHER. NLOS ENVIRONMENTS CONTAIN OBSTRUCTIONS BETWEEN THE TX AND RX

<b>73 GHz Access (RX: 2 m) Manhattan Measurements (TX/RX Antenna Az. HPBW: 7°)</b>		
<b>TX Location (Abbr.) [height]</b>	<b>Environment</b>	<b># of Locations with Signal</b>
Coles Sports Center 1 (COL1) [7 m]	LOS	1 ( $d = 30$ m)
	NLOS	7 ( $53$ m $\leq d \leq 104$ m)
Coles Sports Center 2 (COL2) [7 m]	LOS	1 ( $d = 50$ m)
	NLOS	5 ( $91$ m $\leq d \leq 139$ m)
Kaufman (KAU) [17 m]	LOS	2 ( $48$ m $\leq d \leq 54$ m)
	NLOS	9 ( $59$ m $\leq d \leq 181$ m)
Kimmel Center 1 (KIM1) [7 m]	NLOS	3 ( $50$ m $\leq d \leq 190$ m)
Kimmel Center 2 (KIM2) [7 m]	LOS	1 ( $d = 40$ m)
	NLOS	1 ( $d = 182$ m)
<b>73 GHz Backhaul (RX: 4.06 m) Manhattan Measurements (TX/RX Antenna Az. HPBW: 7°)</b>		
<b>TX Location (Abbr.) [height]</b>	<b>Environment</b>	<b># of Locations with Signal</b>
Coles Sports Center 1 (COL1) [7 m]	NLOS	4 ( $58$ m $\leq d \leq 140$ m)
Coles Sports Center 2 (COL2) [7 m]	NLOS	11 ( $70$ m $\leq d \leq 148$ m)
Kaufman (KAU) [17 m]	LOS	2 ( $49$ m $\leq d \leq 54$ m)
	NLOS	9 ( $59$ m $\leq d \leq 181$ m)
Kimmel Center 1 (KIM1) [7 m]	NLOS	3 ( $50$ m $\leq d \leq 190$ m)
Kimmel Center 2 (KIM2) [7 m]	LOS	2 ( $27$ m $\leq d \leq 40$ m)
	NLOS	1 ( $d = 182$ m)

[61, Fig. 3]. NLOS paths for both receivers were measured when the RX antennas were pointed away from the TX. Several PDPs were recorded over all three T-R separation distances for both RX locations [61], with both the TX and RX antennas pointed zero degrees in elevation (on the horizon). Details pertaining to the measurement hardware are given in Table I and [61].

4) *73 GHz Measurement Descriptions*: The 73 GHz outdoor propagation measurements were conducted in downtown Manhattan around the NYU campus, with a maximum RF transmit power of 14.6 dBm over an 800 MHz first null-to-null RF bandwidth, yielding a maximum measurable dynamic range of 181 dB. The measurements consisted of five TX locations and 27 RX locations with a few of them repeated for more than one TX location, for both base station-to-mobile and backhaul-to-backhaul scenarios. RX antenna heights of 2 m and 4.06 m were used to emulate base station-to-mobile access and wireless backhaul scenarios, respectively. Two TX sites were located on the Coles Sports Center rooftop (7 m above ground level (AGL), with the TX located on the northwest and northeast corners of the roof), two TX sites were placed on the 2nd-floor balcony of the Kimmel center of NYU (7 m AGL, with the TX situated on the northwest and southeast corners of the balcony), and one TX site was located on the fifth-story balcony of the Kaufman Business School (17 m AGL). For each TX location, up to 11 RX locations within 200 meters<sup>§</sup> of the TX were selected, yielding a total of 36 unique mobile access and 38 unique backhaul link measurement combinations (six of the mobile TX-RX combinations and six of the backhaul TX-RX combinations experienced outage over all distances measured). Similar to the approach used in

the 28 GHz measurement campaign, PDPs were recorded using rotatable 27 dBi gain antennas at the TX and RX to capture azimuthal sweeps in 8° (approximately the antenna HPBW) increments using many RX antenna elevation angles for different fixed TX antenna azimuth and elevation angles. In addition, azimuthal TX sweeps were performed with the RX antenna fixed in the azimuth and elevation planes. Up to ten RX azimuthal sweeps and up to two TX azimuthal sweeps were conducted for each TX-RX location combination for both mobile and backhaul measurement scenarios, resulting in up to 540 total PDPs recorded for a single TX-RX location combination. The use of high precision gimbals enabled many more elevation angle measurements at 73 GHz compared to 28 GHz, via a LabVIEW GUI controller that allowed us to easily search and find the strongest received power elevation angles. The specifics of the measurement sweeps and detailed methodology are given in [65]. [75, Fig. 1] shows a map of the TX locations and surrounding RX locations for the 73 GHz measurement campaign. Table III indicates the measurement locations and T-R separation distances where PDPs were recorded at 73 GHz in LOS and NLOS environments for each corresponding TX location and scenario (backhaul or mobile) [41], and Table I provides the channel sounder hardware specifications for all 4 mmWave bands.

### III. DIRECTIONAL PATH LOSS MODELS

#### A. Path Loss Modeling

Since directional, rotatable horn antennas were used for the measurement campaigns in all four mmWave bands (see Table I), we generated path loss and coverage models for directional beamforming, e.g., directional antennas, as well as for omnidirectional antennas (see Section IV). For link budget and interference calculations, path loss as a function of straight

<sup>§</sup>One NLOS T-R separation distance was greater than 200 m (216 m) for both backhaul and mobile measurements, but did not have sufficient received power, thus resulting in an outage.

line 3-D propagation distance is needed for system coverage and interference analysis and design. The relationship between propagation path loss and the 3-D T-R separation distance is based on both the antenna heights and a straight line drawn on a map, passing through obstructions, represented by a single model parameter, the PLE,  $n$ , which describes the attenuation of a signal as it propagates through a channel. Eq. (2) is a fundamental path loss model, usable in LOS and NLOS environments, where  $d_0$  is the close-in free space reference distance:

$$\text{PL}(d)[\text{dB}] = \text{PL}(d_0) + 10\bar{n} \log_{10} \left( \frac{d}{d_0} \right) + X_\sigma, \quad \text{for } d \geq d_0 \quad (2)$$

where  $\text{PL}(d_0)$  is the close in free space path loss (FSPL) in dB, and is a function of wavelength (or frequency) given by  $10 \log_{10} \left( \frac{4\pi d_0}{\lambda} \right)^2$ , with  $d_0 = 1$  m for this work [30], and  $\bar{n}$  is the best fit minimum mean square error (MMSE) PLE over all measurements from a particular measurement campaign.  $X_\sigma$  is a zero mean Gaussian random variable with a standard deviation  $\sigma$  in dB, also known as the shadow factor, representing large-scale signal fluctuations resulting from shadowing by large obstructions in the wireless channel [30]. In previous published mmWave work, our close-in free space reference distance path loss models used various  $d_0$  values such as 3 m [34], 4 m [65], and 5 m [3], [13], depending on different researchers' desires to calibrate the channel sounder in free space using the far-field (Fraunhofer) distance for different directional antennas. In hindsight, standardizing to a reference distance of 1 m would have made comparisons of measurements and models simpler, and would provide a standard definition for the PLE. As shown in this section, the benefit of using a  $d_0 = 1$  m reference distance in (2) provides for easy comparison of various measurement campaigns by different researchers in different environments, and at different frequencies and use cases. In this work, we have recast all of the measurements from the four campaigns (published in [3], [13], [14], [34]–[36], [44], [61], [62], [64], [65]) into path loss models that use  $d_0 = 1$  m as the FSPL anchor point, in order to standardize the use of (2) and to help standards bodies and industry compare their respective models.

As shown in [29], the most substantial difference in path loss across all mmWave bands occurs in the very first meter of propagation from the TX, motivating the use of a 1 m reference distance in (2) for both LOS and NLOS environments. It is a very simple matter to refer any calibrated channel sounder, regardless of antenna gain and Fraunhofer distance, back to a 1 m free space reference distance—one simply extrapolates free space propagation back from the Fraunhofer distance to the 1 m reference distance in the measured path loss data, after free space calibration is performed. We have used such an approach in this paper for all of our measurements, as it both assures that proper far field measurements were conducted, and also provides data for a path loss model using a standardized 1 m close-in free space reference distance.

Emerging mmWave mobile systems will have very few users within a few meters of the antenna (in fact, no users are likely to be in the near field, since transmitters will be mounted on a lamppost or ceiling), and close in users in the near field would have such strong signals or will be power controlled compared

to typical users much farther from the transmitter such that any path loss error in the near-field (between 1 m and the Fraunhofer distance) would be so much smaller than the dynamic range of signals experienced by users in a commercial system. Furthermore, in a typical mobile system with uniformly distributed users, very few users are close to the TX antenna, meaning that propagation model errors close to the TX have minimal impact on system design. Using a reference distance greater than 1 m in (2) is physically plausible for both LOS and NLOS channels, since transmitting antennas are generally mounted in the clear with a large zone of free space around them, and radiation from a TX antenna will experience free space for many meters or tens of meters before encountering clutter, but optimizing for the best reference distance adds model complexity while only reducing the standard deviation by less than a dB in typical outdoor scenarios. Thus, we advocate a standardized 1 m reference distance, even if the calibration distance or free space zone surrounding the TX antenna is greater than 1 m.

An alternative to the close-in free space reference distance path loss model is the *floating intercept*, or *alpha-beta* model of (3) used in the WINNER II and 3GPP channel models [50], [76]. This model has no physical reference or basis, but merely fits the best line to the measured data (via a least-squares regression) to create a floating intercept linear equation model [14], that is only valid over the specific distances for which measurements were made.

$$\text{PL}[\text{dB}] = \alpha + 10 \cdot \beta \log_{10}(d) + X_\sigma \quad (3)$$

In (3),  $\alpha$  is the intercept in dB,  $\beta$  is the slope, and  $X_\sigma$  is a zero mean Gaussian random variable with a standard deviation  $\sigma$  in dB. A common error made by engineers when interpreting path loss models is to assume that  $\beta$  is the same as PLE—it is not.  $\beta$  simply serves to be a particular value of slope that offers the best fit to a scatter plot of data, and has no physical basis or frequency dependence whatsoever [1], [14], [77].  $\beta$  only has a physical meaning, like PLE, when  $\alpha$  is set equal to the free space reference distance close to the antenna. As discussed in [14] and [48], the standard deviation is reduced by only 1 dB or so when using (3) instead of using (2) with  $d_0 = 1$  m, yet there is no physical basis for (3), and different researchers cannot immediately extract insightful information from two model parameters,  $\alpha$  or  $\beta$ . Given that both (2) and (3) typically have 7 to 12 dB of standard deviation (not a terribly good model, albeit a simple one), we believe it makes sense to use a single parameter model for  $d_0 = 1$  m in (2) [48], rather than to have every propagation researcher create their own model where  $\alpha$  and  $\beta$  have no physical relevance.

Both the close-in free space reference distance model and floating intercept model may be used to characterize mmWave channels in both LOS and NLOS environments, but we advocate the use of (2) with  $d_0 = 1$  m for mmWave path loss channel modeling, because of the simpler form, the physical basis, and the additional benefit of having an agreed-upon standard that is usable with reasonable accuracy across many environments, scenarios, and frequency bands.

While early cellular UHF models used 1 km or 100 m as the  $d_0$  reference distance due to tall base station antennas that were “in the clear” and provided larger cell sizes, 1 m is more relevant for mmWave since there are generally no obstructions

TABLE IV  
PATH LOSS TERMINOLOGY FOR DIRECTIONAL PATH LOSS MODELS

Setting	Description
LOS	Path loss when the TX and RX antennas are pointed at each other, aligned on boresight, with no obstructions between them.
NLOS	Path loss when the TX and RX antennas are separated by obstructions and there is no clear optical path between the antennas. This scenario also includes the case where the TX and RX antennas have a clear line-of-sight path to one another, but the antennas are not aligned on boresight.
NLOS-best	Path loss for the unique antenna pointing angles (in the azimuth and elevation planes) resulting in the strongest received power for each specific TX-RX location combination. This results from the single strongest measured PDP from the NLOS data at each TX-RX location combination.

around antennas within the first meter, and cell sizes will have radii up to a few hundred meters [1], [30].

B. Mobile Access and Backhaul Directional Close-in Free Space Reference Distance Path Loss Models

The directional propagation models for 28, 38, and 73 GHz based on our measurements were formed from all measured antenna pointing angles between the TX and RX antennas. Base station-to-mobile (access) measurements were conducted at 28, 38, and 73 GHz, and base station-to-base station (backhaul) measurements were conducted at 73 GHz. Table IV describes the terminology used for directional path loss models. Fig. 1 shows measured data and close-in free space reference distance ( $d_0 = 1$  m) directional path loss models for the 73 GHz hybrid (RX heights of 4.06 and 2 m) measurements, for each setting described in Table IV. Fig. 1 plots path loss obtained by integrating the power under PDPs obtained from all of the individual unique antenna pointing angles between the TX and RX over all measurements. The close-in free space reference distance  $d_0 = 1$  m yields 69.8 dB path loss in the first meter of propagation at an RF carrier frequency of 73.5 GHz, and is the y-axis anchor point for the MMSE fit.

Table V provides the close-in free space reference distance ( $d_0 = 1$  m) directional path loss models of (2) for the different 28, 38, and 73 GHz campaigns. The LOS PLE for the 28 and 38 GHz campaigns are comparable, as they are  $\bar{n} = 1.9$ . The smaller  $\sigma$  value for 28 GHz LOS measurements can be attributed to different channel types (NYC vs. Austin) as compared to 38 GHz measurements. As for the 73 GHz LOS PLE being approximately  $\bar{n} = 2.3$  for all scenarios, this can be attributed to the difficulty in aligning very narrowbeam directional horn antennas perfectly on boresight for the T-R separation distances measured, and this indicates the sensitivity of beam pointing in future mmWave wireless systems. To improve LOS field measurements, laser pointers can be used to ensure boresight alignment, or a power-alignment scheme between the TX and RX antennas may be employed. Overall, the LOS PLEs for the 28, 38, and 73 GHz measurements compare well with the theoretical FSPL of  $n = 2$  (20 dB of attenuation per decade of distance).

For NLOS conditions with narrowbeam antennas, the 38 GHz campaign had the smallest (least lossy) directional PLE of 3.3, compared to 4.5 for 28 GHz and 4.7 for all 73 GHz channels. The UTA measurements only looked for

73 GHz Directional Path loss vs. Distance in Manhattan with RX Height: 2 m & 4.06 m  
Using 27 dBi, 7° 3dBi BW TX and RX Antennas

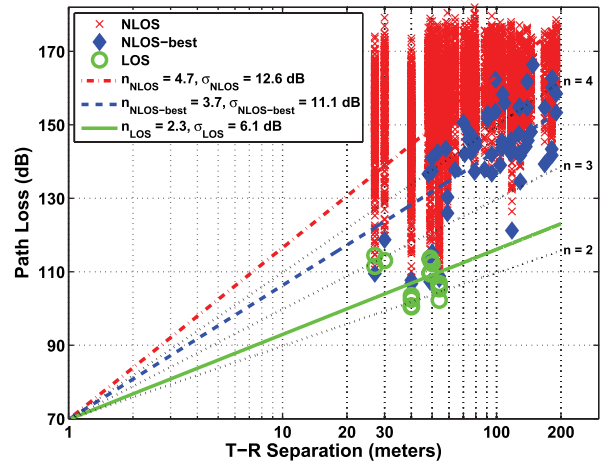


Fig. 1. 73 GHz directional close-in free space reference distance ( $d_0 = 1$  m) path loss models for the hybrid scenario with RX antenna heights of 2 m and 4.06 m in Downtown New York City. Each red cross represents NLOS path loss values measured at each unique antenna pointing angle between the TX and RX (provided signal could be received), blue diamonds represent the particular TX-RX pointing angle that resulted in the lowest path loss measured for each specific NLOS TX-RX location combination, and green circles represent LOS path loss values.

strong paths (stronger than were encountered on the antenna sweeps at 28 and 73 GHz), and the campus has more foliage, more undulating terrain, and is less urban than New York City, thus the transmitted signal did not encounter as many blockages in the propagation channel. The shadow factor or standard deviation about the mean path loss line is comparable for all three frequency bands, around 10 dB, although the standard deviation increases with carrier frequency. The 73 GHz NLOS PLEs for each TX height scenario are all larger than the narrowbeam and widebeam NLOS PLEs at 28 GHz, and are also greater than the narrowbeam and widebeam NLOS PLEs at 38 GHz in Austin. Because 73 GHz signals have shorter wavelengths than 28 GHz and 38 GHz, the propagating wave attenuates more as it encounters rough surfaces of buildings that cause diffuse scattering, as well as undergoing 8.3 dB more path loss in the first meter of free space propagation compared to 28 GHz.

As presented in Table IV, the NLOS-best setting is for the single strongest received power antenna pointing angle orientation between the TX and RX antennas for each NLOS TX-RX location combination (i.e. the lowest measured path loss for each location). That is, NLOS-best is equivalent to directional beamforming (BF) using the best single beam at both the TX and RX. From the measured path loss values at each location an MMSE NLOS-best line is fit to the NLOS data to generate models following (2). Path loss models, when considering the strongest received power pointing angles, show a decrease in attenuation (much better coverage), compared to the arbitrary pointing angle models at each frequency. Future mmWave adaptive array algorithms will be used to determine these preferred pointing angles at both the TX and RX [1], [6], [78]. When using the single strongest beam angles, Table V shows the PLE reduces by 7 dB, 6 dB, and 10 dB per decade of distance for the 28 GHz, 38 GHz, and 73 GHz NLOS narrowbeam measurements, respectively, compared to

TABLE V

DIRECTIONAL CLOSE-IN FREE SPACE REFERENCE DISTANCE ( $d_0 = 1$  m) PATH LOSS MODELS (EQ. (2)) FOR BASE STATION-TO-MOBILE (ACCESS) AND BASE STATION-TO-BASE STATION (BACKHAUL) SCENARIOS. PLE IS THE PATH LOSS EXPONENT AND  $\sigma$  IS THE STANDARD DEVIATION OF THE ZERO-MEAN GAUSSIAN RANDOM VARIABLE (SHADOW FACTOR). HPBW IS THE 3 dB BEAMWIDTH OF THE TX AND RX ANTENNAS,  $G$  IS THE GAIN OF EITHER THE TX OR RX ANTENNA, AND  $h$  IS THE HEIGHT ABOVE GROUND OF EITHER THE TX OR RX ANTENNA. THE 2 m, 4.06 m, AND COMBINED 2 m AND 4.06 m RX HEIGHTS FOR THE 73 GHz MEASUREMENTS ARE THE ACCESS, BACKHAUL, AND HYBRID SCENARIOS, RESPECTIVELY

Directional Close-in Reference Distance Path Loss Models for $d_0 = 1$ m										
	TX/RX HPBW (°)	$G_{TX}/G_{RX}$ (dBi)	$h_{TX}$ (m)	$h_{RX}$ (m)	LOS		NLOS		NLOS-best	
					PLE	$\sigma$ [dB]	PLE	$\sigma$ [dB]	PLE	$\sigma$ [dB]
28 GHz (Man.)	10.9 / 10.9	24.5 / 24.5	7; 17	1.5	1.9	1.1	4.5	10.0	3.8	9.3
28 GHz (BK.)	28.8 / 10.9	15 / 24.5	40		-	-	4.1	7.1	3.5	3.3
38 GHz (Austin)	7.8 / 7.8	25 / 25	8; 23; 36	1.5	1.9	4.6	3.3	12.3	2.7	10.2
	7.8 / 49.4	25 / 13.3			1.9	3.5	2.8	10.3	2.4	7.9
73 GHz (Man.)	7 / 7	27 / 27	7; 17	2	2.2	5.2	4.7	12.6	3.6	10.6
				4.06	2.4	6.3	4.7	12.7	3.7	11.2
				2; 4.06	2.3	6.1	4.7	12.6	3.7	11.1

TABLE VI

DIRECTIONAL FLOATING INTERCEPT PATH LOSS MODELS AT 28 GHz, 38 GHz, AND 73 GHz.  $\alpha$  IS THE FLOATING INTERCEPT,  $\beta$  IS THE SLOPE OF THE LEAST SQUARES LINE, AND  $\sigma$  IS THE STANDARD DEVIATION OF THE ZERO-MEAN GAUSSIAN RANDOM VARIABLE (SHADOW FACTOR) ABOUT THE LEAST SQUARES LINE

Directional Floating Intercept ( $\alpha$ - $\beta$ ) Path Loss Models													
	TX/RX HPBW (°)	$G_{TX}/G_{RX}$ (dBi)	$h_{TX}$ (m)	$h_{RX}$ (m)	LOS			NLOS			NLOS-best		
					$\alpha$ [dB]	$\beta$	$\sigma$ [dB]	$\alpha$ [dB]	$\beta$	$\sigma$ [dB]	$\alpha$ [dB]	$\beta$	$\sigma$ [dB]
28 GHz (Man.)	10.9 / 10.9	24.5 / 24.5	7; 17	1.5	45.3	2.9	0.04	57.6	4.7	10.0	41.2	4.7	8.9
28 GHz (BK.)	28.8 / 10.9	15 / 24.5	40		-	-	-	144.7	0.2	7.1	158.2	-1.1	2.2
38 GHz (Austin)	7.8 / 7.8	25 / 25	8; 23; 36	1.5	68.8	1.7	4.4	125.4	0.55	8.3	107.8	0.8	7.8
	7.8 / 49.4	25 / 13.3			73.3	1.5	3.1	108.4	0.80	7.3	92.3	1.1	6.3
73 GHz (Man.)	7 / 7	27 / 27	7; 17	2	126.2	-1.2	4.4	122.6	1.8	11.2	43.2	4.9	10.3
				4.06	126.2	-1.1	4.8	114.2	2.3	11.5	34.6	5.5	10.6
				2; 4.06	127.9	-1.2	4.6	118.2	2.1	11.3	38	5.3	10.5

arbitrary pointing angles. This reduction in attenuation is significant and motivates beam combining and beamforming at mmWave frequencies in order to improve link margin and SNR, and can also result in lower RMS delay spreads [1], [44], [49], [64], [72]. Antenna beamwidth at the RX also impacts the received signal level, as Table V shows that 38 GHz PLEs are lower for widebeam RX antennas, as they were able to capture energy in a wider azimuth spread than narrowbeam antennas in a NLOS setting, but did not capture signals with high path loss due to the smaller antenna gain. This reduces the dynamic range of the measurement system (due to lower antenna gains) compared to the use of narrowbeam RX antennas. A comprehensive list of the minimum, average, and maximum directional path loss values for each NLOS TX-RX combination, as well as RMS delay spread data, tested for the 28 GHz and 73 GHz campaigns are given in [49].

### C. Mobile Access and Backhaul Directional Floating Intercept Path Loss Models

The floating intercept model of Eq. (3) is a least squares fit to the propagation data without a constraint, over the range of measurement distances, but does not have a physical basis because there is no physically-based anchor point like in the close-in reference distance model (2). The close-in free space reference distance model can be extended past the measured T-R separation distances because it is referenced to a known FSPL; however, the floating intercept model cannot, since (3) is a best fit line to a set of data with a form similar to Eq. (2), but with no physical basis for the values of  $\alpha$  and  $\beta$ .

For the 28 and 73 GHz campaigns, T-R separation distances ranged from approximately 50 to 200 m for the NLOS floating intercept model, whereas the 38 GHz measurements had distances ranging from 29 m to more than 900 m. The floating intercept model finds a slightly better fit to measured data without a constraint and usually results in a slightly lower standard deviation (shadow factor:  $\sigma$ ) about the best fit line on a scatter plot, although in most cases the difference is much less than 1 dB [14], [38], [94].

The values in Table VI have no physical basis as is clearly seen by the fact that some of the best fit line slopes  $\beta$  are close to zero or even negative, caused by fitting a least squares line over a large range of path loss values measured over many T-R separation distances [14]. In some cases, the slope ( $\beta$ ) of the best fit line for NLOS pointing angles with the strongest power is larger than the close-in reference distance PLE for the NLOS-best models. The floating intercept model is also very sensitive, such that even changing some post-processing techniques or noise floor thresholding can significantly change the values computed for these unique pointing angle models; therefore, at mmWave frequencies, we propose to use the close-in free space reference distance model with a 1 m reference distance due to its physical basis, stability, and the benefit of having a standard model to compare many measurements and scenarios from groups worldwide.

## IV. OMNIDIRECTIONAL PATH LOSS MODELS

Directional path loss models are important for systems using narrowbeam directional antennas since mmWaves will take advantage of beamforming and beam combining techniques [49].

However, standards bodies have historically been interested in omnidirectional models, especially for NLOS channels, since all legacy wireless systems have used quasi-omnidirectional antennas at the user equipment (UE), and arbitrary antenna patterns and MIMO processing may be easily analyzed and simulated with omnidirectional models. In this section, omnidirectional close-in free space reference distance ( $d_0 = 1$  m) path loss and floating intercept models are presented. The raw data used to compute omnidirectional path loss models at 28, 38 and 73 GHz are provided in tabular form in [94]. To create these models, the received power from unique pointing angle combinations between the TX and RX antennas for each TX-RX location combination were synthesized. Originally, directional measurements were made for  $i$  TX locations and  $j$  RX locations for arbitrary TX antenna pointing angles  $\theta_t$  and  $\phi_t$  in the azimuth and elevation planes, respectively, and for arbitrary RX antenna pointing angles  $\theta_r$  and  $\phi_r$  in the azimuth and elevation planes, respectively. Received power (or area under a PDP) was measured at every unique TX and RX azimuth/elevation antenna pointing angle combination for every distinct TX-RX location pair. The  $\theta$  and  $\phi$  angle values for every distinct pointing angle combination correspond to received power  $\widetilde{Pr}_{i,j}(\theta_r, \phi_r, \theta_t, \phi_t)$  for every directional measurement. TX and RX antenna gains (in dB) were removed for each received power level  $\widetilde{Pr}_{i,j}(\theta_r, \phi_r, \theta_t, \phi_t)$  such that  $Pr_{i,j}(\theta_r, \phi_r, \theta_t, \phi_t) = \widetilde{Pr}_{i,j}(\theta_r, \phi_r, \theta_t, \phi_t) - G_{TX} - G_{RX}$ . Then for each distinct TX-RX location combination measured, the received powers for each and every unique TX and RX azimuth and elevation angle combination (with antenna gains removed) were summed together in linear scale (mW) to recover an omnidirectional received power from which an omnidirectional path loss model was computed. The omnidirectional received power can be synthesized in this way because each narrowbeam angle spread measured over the entire  $4\pi$  steradian sphere can be regarded as an orthogonal non-overlapping spatial segment, obviating the need to de-embed the antenna pattern when calculating the omnidirectional received power. We proved the accuracy of this approach by carefully studying and comparing the summed versions of adjacent directional measurements that were separated by HPBW increments. Additionally, the measured data at 28 GHz showed that using nine adjacent  $10.9^\circ$  HPBW antennas in the azimuth and elevation plane yields virtually identical received power (area under the PDP) as using one  $28.8^\circ$  HPBW antenna (where the HPBW of the widebeam antenna is about three times that of the narrowbeam antenna), which further validates the synthesizing method. Thus, for each TX-RX location pair, omnidirectional path loss was recovered from the unique pointing angle received powers using

$$PL_{i,j}[\text{dB}] = Pt_{i,j}[\text{dBm}] - 10 \log_{10} \left[ \sum_z \sum_y \sum_x \sum_w Pr_{i,j}(\theta_{r_w}, \phi_{r_x}, \theta_{t_y}, \phi_{t_z}) [\text{mW}] \right] \quad (4)$$

where  $Pt_{i,j}$  is the transmit power in dBm. A more detailed description of how the directional measurements were aggregated together to create omnidirectional models similar to those in [39] and [40] was presented in [38]. The LOS and NLOS ter-

TABLE VII  
PATH LOSS TERMINOLOGY FOR OMNIDIRECTIONAL PATH LOSS MODELS

Setting	Description
LOS	Path loss when there is a clear optical path between the TX and RX site.
NLOS	Path loss when the TX and RX sites are separated by obstructions and there is no clear direct path between the antennas.

minology for the omnidirectional model follows the traditional sense and is explained in Table VII.

The omnidirectional close-in free space reference distance path loss models are presented for LOS and NLOS environments as described by parameters in Table VIII, along with a NLOS floating intercept model. Fig. 2 shows the omnidirectional LOS and NLOS close-in reference distance ( $d_0 = 1$  m) FSPL models and the NLOS floating intercept model for the 73 GHz hybrid scenario. The LOS PLE for the hybrid case is  $\bar{n} = 2$ , consistent with theoretical FSPL of 20 dB per decade of distance. The standard deviation about the mean FSPL line is relatively low at 4.8 dB. The computed NLOS PLE was 3.4 meaning that with omnidirectional and isotropic 0 dBi gain antennas at the TX and RX, a 73 GHz wideband signal will attenuate by 34 dB per decade of distance. Fig. 2 also shows the omnidirectional NLOS floating intercept model with a slope of 2.9 and standard deviation of 7.8 dB, only 0.1 dB less than the close-in reference NLOS omnidirectional FSPL model, showing that the *alpha-beta* model does not meaningfully reduce the standard deviation. While the slope of the NLOS floating intercept model is lower than the close-in reference distance PLE, it is only valid over the  $\sim 50$  m to 200 m measurement range. A path loss model at 1.9 GHz for the NLOS environment in San Francisco using omnidirectional antennas with a base station antenna height of 3.7 m and a mobile RX antenna height of 1.7 m is also displayed in Fig. 2 with a PLE of 2.6 and a standard deviation of 7.7 dB [79]. This comparison to the 73 GHz path loss line shows that the PLEs are not vastly different. The difference lies in both the additional free space path loss in the first meter of propagation attributed by Friis' free space path loss equation where path loss is proportional to the square of the carrier frequency, as well as additional attenuation by the environment at mmWave frequencies. Fig. 2 shows that 8 dB per decade of distance more loss is experienced at 73 GHz than at 1.9 GHz. This difference in the propagation at mmWaves can be made up by using directional, high gain antennas in addition to beamforming and beam combining techniques [49], [64].

Given the omnidirectional path loss parameters for 28, 38, and 73 GHz in Table VIII, it is apparent that the LOS PLEs are almost identical to true FSPL of  $n = 2$ . The NLOS omnidirectional PLEs are significantly lower compared to the directional models, where for 28 GHz measurements the NLOS omnidirectional path loss is 11 dB and 6 dB per decade of distance lower compared to the narrowbeam and widebeam directional cases, respectively. At 38 GHz, the NLOS omnidirectional path loss is 5 dB and 4 dB per decade of distance lower compared to the narrowbeam and widebeam models, respectively. The greatest difference between directional and omnidirectional path loss models is at 73 GHz. The access, backhaul, and hybrid NLOS omnidirectional path loss values are all 10 dB per decade of

TABLE VIII  
 OMNIDIRECTIONAL CLOSE-IN FREE SPACE REFERENCE DISTANCE ( $d_0 = 1$  m) AND FLOATING INTERCEPT PATH LOSS MODELS FOR ALL MEASURED DATA FOR BASE STATION-TO-MOBILE (ACCESS) AND BASE STATION-TO-BASE STATION (BACKHAUL) SCENARIOS.  $\alpha$  IS THE FLOATING INTERCEPT,  $\beta$  IS THE SLOPE OF THE MMSE LINE, AND  $\sigma$  IS THE STANDARD DEVIATION OF THE ZERO-MEAN GAUSSIAN RANDOM VARIABLE (SHADOW FACTOR) ABOUT THE LEAST SQUARES BEST FIT LINE FOR THE RANGE OF DISTANCES SPECIFIED FOR EACH FREQUENCY BAND. MAN. STANDS FOR MANHATTAN

Omnidirectional Path Loss Models ( $d_0 = 1$ m)											
	TX/RX scenario	TX Ht. (m)	RX Ht. (m)	NLOS Meas. Range: d (m)	LOS		NLOS		NLOS (Floating)		
					PLE	$\sigma$ [dB]	PLE	$\sigma$ [dB]	$\alpha$ [dB]	$\beta$	$\sigma$ [dB]
28 GHz (Man.)	Narrow/Narrow	7; 17	1.5	$61 \leq d \leq 187$	2.1	3.6	3.4	9.7	79.2	2.6	9.6
38 GHz (Austin)	Narrow/Narrow	23	1.5	$61 \leq d \leq 150$	2.0	2.4	2.8	9.1	39.1	4.0	8.9
				$75 \leq d \leq 377$	1.9	3.6	2.6	10.8	122.2	0.1	9.2
				$61 \leq d \leq 377$	1.9	3.4	2.7	10.5	100.9	1.0	9.6
				$29 \leq d \leq 377$	1.9	4.4	2.7	10.1	96.2	1.3	9.1
	Narrow/Wide	23	1.5	$d = 101$	1.8	2.4	2.6	-	-	-	-
				$75 \leq d \leq 728$	1.8	1.8	2.2	4.1	81.7	1.5	3.4
				$75 \leq d \leq 728$	1.8	2.1	2.3	4.9	88.6	1.2	3.4
				$29 \leq d \leq 728$	1.8	3.2	2.3	7.4	88.2	1.3	5.7
73 GHz (Man.)	Access	7; 17	2	$48 \leq d \leq 190$	2.0	5.2	3.3	7.6	81.9	2.7	7.5
	Backhaul		4.06	$50 \leq d \leq 190$	2.0	4.2	3.5	7.9	84.0	2.8	7.8
	Hybrid		2; 4.06	$48 \leq d \leq 190$	2.0	4.8	3.4	7.9	80.6	2.9	7.8

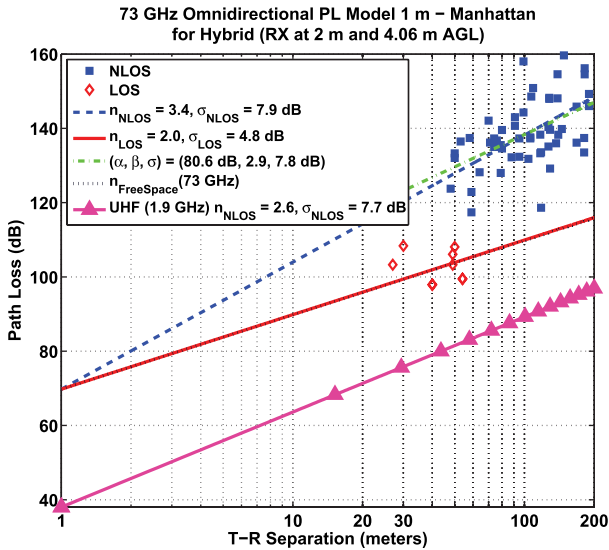


Fig. 2. 73 GHz omnidirectional close-in free space reference distance ( $d_0 = 1$  m) and floating intercept (NLOS) path loss models for the hybrid scenario with RX antenna at heights of 2 m and 4.06 m in New York City. Blue squares represent NLOS omnidirectional path loss values and red diamonds represent LOS omnidirectional path loss values. An omnidirectional NLOS path loss model for the 1.9 GHz band measured in San Francisco is also displayed on the figure for comparison [79].

distance lower than their respective directional models. The 73 GHz campaign had a larger data set and explored many more azimuth and elevation plane combinations between the transmit and receive antennas that were used to create the omnidirectional model, perhaps resulting in a more accurately synthesized model. With more narrowbeam measurements in the azimuth and elevation planes at 28 and 38 GHz, we would expect the omnidirectional PLEs to be slightly lower compared to their respective directional PLEs, like in the 73 GHz cases. We note that the data suggests PLE tends to increase slightly with frequency in a given environment, meaning that higher mmWave frequencies experience slightly more loss per distance due to the environment (in addition to the dominant first

meter free space loss). This is most likely due to more rough surface/diffuse scattering and less reflectivity in the physical environment as the wavelength shrinks.

Similar to the directional floating intercept path loss models, the omnidirectional floating intercept path loss models have no physical basis. As noticed for the NLOS directional floating intercept models, the NLOS omnidirectional floating intercept models also reveal a small reduction in the shadow factor ( $\sigma$ ), but the changes are minimal (typically less than one dB). In addition, the floating intercept model is only valid over the T-R separation distances measured during the campaign, whereas the close-in free space reference distance model can be extended, due to its physical basis, to distances farther than the measurement range. The floating intercept model parameters for the 28 and 73 GHz campaigns are slightly different here than those described in [40], due to an updated PDP thresholding algorithm that uses a more stringent 5 dB SNR threshold, and by separating the TX-RX path loss data points by RX antenna height, as described in [38]. The values in Table VIII can be used to model the propagation environment, using simple equations with a 1 m free space reference distance as shown for the general form in Eq. (5).

$$PL(\text{envr}, f_c, d)[\text{dB}] = \text{FSPL}(f_c, d_0 = 1) + \overline{n}_{\text{envr}, f_c} \cdot 10 \log_{10}(d) + X_\sigma(\text{envr}, f_c)[\text{dB}] \quad (5)$$

where:

$$\text{FSPL}(f_c, d_0 = 1)[\text{dB}] = 20 \log_{10} \left( \frac{4\pi}{c/f_c} \right) \quad (6)$$

for distances  $d$ , speed of light  $c$  and the environment (envr), whether LOS or NLOS, and for the appropriate carrier frequency,  $f_c$ . The omnidirectional models presented here are useful for mmWave standards bodies and have not been previously presented over so many frequency bands in a unified format.

Using (5) and data such as given in Table VIII, the optimum averaged PLE value in (2) can be found for an operating environment (e.g, LOS or NLOS) or scenario (e.g., UMi or UMa) over many frequencies and distances by computing the path loss, in dB, for each measurement campaign (table entry),

and then subtracting out the 1 m free space path loss for each campaign. It is important to compute the PLE in (2) based on the propagation beginning at 1 m (with the first meter of free space path loss subtracted out), and to not be tempted to simply average PLE values across frequencies, since the first meter of propagation can induce 32 to 72 dB of loss from 1 to 100 GHz. In other words, the first meter of propagation has an important, physically-based frequency-dependent effect that should not be averaged, but should be represented separately as shown in (5), where the PLE represents the environmental effects of propagation (which become slightly more lossy at higher mmWave frequencies). Solving for the optimum PLE in (2) is done by subtracting the first meter of free space propagation loss from the path loss data, and then finding a MMSE fit on all of the path loss data (with 1 m free space loss removed) over all frequencies and distances simultaneously. Using (2) for a particular operating environment or scenario can provide an accurate, stable, robust, and yet very simple path loss model over a wide range of mmWave frequencies. The simple, one parameter close-in free space reference distance path loss model given by (2) and (5) could be of value to standard bodies, since it is physically based and standardizes around an inherent 1 m free space reference distance that is frequency dependent. Optimizing (2) to find the best-fit close-in reference distance, or using a table lookup procedure for PLE values at different frequencies, or using a PLE value that is a function of frequency and/or distance to minimize the shadowing standard deviation, and adding loss parameters to account for the environment or frequency are all possible variations of the close-in free space reference distance model. More measurements, however, are needed to validate its accuracy in comparison to other models.

## V. BEAM COMBINING

As the mmWave wideband regime continues to grow, it is apparent that the number of antenna elements on a device will increase as the RF carrier frequency increases. In conjunction with this, high gain directional antennas are envisaged as crucial elements in order to detect mmWave signals with reasonable SNR. Since devices will employ very directional, high gain antennas, beam combining techniques and beamforming algorithms will need to be developed to actively search for and find the strongest departing and incoming directional beams at the TX and RX, respectively [49], [64]. By determining the strongest received power angle combinations, multiple antenna elements can be used to increase the SNR of the incoming signal, and may reduce the path loss observed at the RX, compared to any arbitrary antenna pointing angle. Work presented in [44], [64], [72] shows the reduction in PLEs when combining the few strongest beam powers at the RX for 28 and 73 GHz for both coherent and non-coherent beam combining. Reducing the PLE is synonymous with extending the coverage distance of a cell. While the results in [44], [64], [72] showed beam combining for different reference distances and for the NLOS environments described in Table IV, here we present all beam combining results following the NLOS descriptions presented in Table VII (does not include non-boresight LOS measurements) with respect to a 1 m close-in free space reference distance.

Beam combining may be performed coherently or non-coherently. Most current wireless systems are coherently based; however, this does not mean that future 5G and mmWave systems will necessarily be coherent. Coherent beam combining assumes multipath components at different angles can be time-aligned and is performed by taking the square root of the strongest individual total received powers in Watts from PDPs recorded for a given TX-RX link, summing together the equivalent voltages, and then squaring the summed result. Only unique angle combinations are used here such that the same beam is not considered twice. The method for determining received power for coherent beam combining is shown in Eq. (7):

$$P_{\text{coherent}} = \left( \sum_{i=1}^N \sqrt{P_i} \right)^2 \quad (7)$$

where  $P_i$  are the individual strongest received powers from unique TX-RX antenna pointing angle combinations, and  $N$  is the number of strongest beams considered. Non-coherent beam combining assumes detection of each unique beam and then sums the received powers in Watts of the strongest beam combinations:

$$P_{\text{non-coherent}} = \sum_{i=1}^N P_i \quad (8)$$

Combining the strongest directional beams for each NLOS TX-RX location combination results in reduced PLEs and shadow factors as presented in Table IX, and are all with respect to a 1 m close-in free space reference distance. Table IX also shows *distance extension exponents* (DEEs) used to determine the extended distance where a user would experience the same path loss for combining the best beams compared to the single best beam [41], [44], [72], and is shown in (9), where  $d$  denotes the coverage distance:

$$d_{(\text{multibeam})} = \left[ d_{(1 \text{ beam})} \right]^{\text{DEE}} \quad (9)$$

where the path loss experienced at a distance  $d_{(1 \text{ beam})}$  for the single best beam, is the same path loss experienced at a distance  $d_{(\text{multibeam})}$  when combining multiple beams, and is determined using the DEEs specified in Table IX.

From the results in Table IX [1] it is obvious that coherently combining the beams with the strongest measured powers for a particular location reduces the PLE more than non-coherently combining. When coherently combining beams, the resulting PLE may sometimes be lower than the omnidirectional PLE. Non-coherent combining is the same procedure used for determining the omnidirectional path loss models shown in Table VIII (simply summing the powers), and it is expected that the non-coherent PLE would converge to the omnidirectional PLE as the number of beams increases. When comparing the PLE for any arbitrary pointing angle with respect to (w.r.t.) a 1 m close-in free space reference distance versus coherently combining the four best unique beams to determine the PLE, significant reductions in the PLE are noticed for all frequency bands, but the distance extension effect as defined in [41] may not be apparent. For instance, the path loss observed at 200 meters for the single (strongest) best measured beam at 28 GHz is also observed at a distance of 450 m when coherently combining the four strongest measured beams,

TABLE IX

DIRECTIONAL CLOSE-IN FREE SPACE REFERENCE DISTANCE ( $d_0 = 1$  m) BEAM COMBINING PATH LOSS MODELS AT 28 GHz, 38 GHz, AND 73 GHz IN NLOS ENVIRONMENTS. *PLE* IS THE PATH LOSS EXPONENT,  $\sigma$  IS THE STANDARD DEVIATION OF THE ZERO-MEAN GAUSSIAN RANDOM VARIABLE (SHADOW FACTOR) ABOUT THE MMSE LINE, *Beams* IS THE NUMBER OF MEASURED BEAMS USED FOR THE COHERENT AND NON-COHERENT BEAM COMBINING PROCEDURE, AND DEE [41] IS THE *Distance Extension Exponent* USED TO DETERMINE THE EXTENDED COVERAGE DISTANCE WHEN COMBINING MULTIPLE BEAMS. THE ARBITRARY POINTING ANGLE PLES ARE ALSO DISPLAYED FROM TABLE V TO COMPARE THE MODELS FOR BEST (STRONGEST MEASURED) BEAMS AND ANY ARBITRARY BEAM

NLOS Directional Beam Combining Path Loss Models ( $d_0 = 1$ m)										
Frequency	TX Height (m)	RX Height (m)	TX / RX Antenna HPBW							
28 GHz (Man.)	7; 17	1.5	10.9° / 10.9°	PLE (Over all angles) = 4.556						
				Coherent		Non-Coherent				
				Beams	PLE	$\sigma$ [dB]	DEE	PLE	$\sigma$ [dB]	DEE
				1	3.812	9.1	-	3.812	9.1	-
				2	3.548	9.1	1.074	3.692	9.2	1.033
				3	3.406	9.2	1.119	3.631	9.2	1.050
				4	3.307	9.2	1.153	3.591	9.2	1.062
38 GHz	8; 23; 36	1.5	7.8° / 7.8°	PLE (Over all angles) = 3.295						
				Coherent		Non-Coherent				
				Beams	PLE	$\sigma$ [dB]	DEE	PLE	$\sigma$ [dB]	DEE
				1	2.801	12.2	-	2.801	12.2	-
				2	2.653	10.9	1.056	2.756	11.5	1.016
				3	2.579	10.6	1.086	2.741	11.4	1.022
				4	2.531	10.3	1.107	2.731	11.3	1.026
				7.8° / 49.4°	PLE (Over all angles) = 2.826					
		Coherent			Non-Coherent					
		Beams	PLE		$\sigma$ [dB]	DEE	PLE	$\sigma$ [dB]	DEE	
		1	2.588		8.9	-	2.588	8.9	-	
		2	2.363	7.9	1.095	2.497	8.3	1.036		
3	2.257	7.3	1.147	2.461	7.9	1.052				
4	2.191	6.9	1.182	2.443	7.8	1.060				
73 GHz	7; 17	2	7° / 7°	PLE (Over all angles) = 4.687						
				Coherent		Non-Coherent				
				Beams	PLE	$\sigma$ [dB]	DEE	PLE	$\sigma$ [dB]	DEE
				1	3.728	7.6	-	3.728	7.6	-
				2	3.466	7.3	1.076	3.613	7.4	1.032
				3	3.327	7.2	1.121	3.557	7.3	1.048
				4	3.235	7.2	1.152	3.523	7.3	1.058
				4.06	PLE (Over all angles) = 4.660					
		Coherent			Non-Coherent					
		Beams	PLE		$\sigma$ [dB]	DEE	PLE	$\sigma$ [dB]	DEE	
		1	3.823		8.9	-	3.823	8.9	-	
		2	3.578	8.5	1.067	3.718	8.6	1.028		
		3	3.446	8.1	1.110	3.667	8.3	1.043		
		4	3.353	7.8	1.140	3.632	8.1	1.053		
		2; 4.06	PLE (Over all angles) = 4.675							
			Coherent		Non-Coherent					
			Beams	PLE	$\sigma$ [dB]	DEE	PLE	$\sigma$ [dB]	DEE	
			1	3.779	8.4	-	3.779	8.4	-	
2	3.578		8.0	1.072	3.670	8.1	1.030			
3	3.446		7.7	1.115	3.616	7.9	1.045			
4	3.353	7.6	1.146	3.582	7.8	1.055				

corresponding to a DEE of 1.153 [41]. The *distance extension factor* (DEF) was also derived in [41] that resulted in a DEF of 2.25 when coherently combining the four single strongest measured beams at 28 GHz. The reduced PLEs for the 38 GHz campaign are not as significant as the 28 GHz and 73 GHz campaigns because fewer measurements were made (perhaps because only one or two substantially strong beams were detected at some locations) and the environment was less cluttered, meaning that a smaller number of MPCs would reach the RX with significant energy. As shown in Tables V and IX, the PLEs determined through antenna beam searching and combining are much smaller than the PLEs for pointing antennas in arbitrary directions, and this is an important fact

for mmWave 5G communications systems. Note that the angular search for power in the 28 GHz and 38 GHz measurements was less extensive than at 73 GHz, where a larger portion of the  $4\pi$  steradian sphere was measured. It should also be noted that we systematically found the strongest received power angle combinations between the TX and RX antennas at 73 GHz such that our measurements sweeps covered the azimuth and elevation planes with the most energy. Overall, these results show that for any mmWave band, coherently combining beams can significantly improve the SNR of the received signal as seen in Table IX, where coherently combining the best four beams for the 73 GHz case with a 2 m RX height reduces the signal attenuation by approximately 14.5 dB per

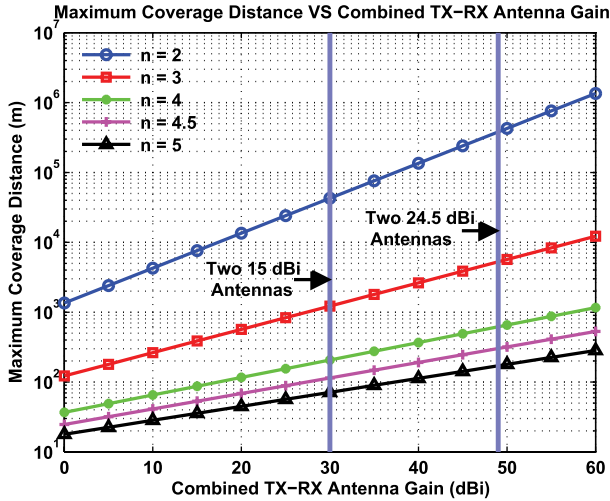


Fig. 3. Maximum coverage distance at 28 GHz for a system with 129 dB maximum measurable path loss (with 0 dBi gain antennas at the TX and RX) and a 5 dB SNR as a function of the TX and RX antenna gains, for PLEs ranging from two to five. The two solid vertical lines correspond to 15 dBi and 24.5 dBi antennas used at both the TX and RX in the 28 GHz outdoor measurements [3].

decade of distance. Reducing the PLE extends the coverage distance or increases SNR that enables higher order modulation constellations [1].

High gain directional antennas are a departure from today’s cellular systems that generally use omnidirectional receivers at the handset and widebeam antennas at the base station. More flexibility exists for systems at mmWave frequencies to use many more high gain directional antennas, because the form factor is so much smaller at higher frequencies [1], [4], [5], [34], [78]. Fig. 3 modified from [3] displays the maximum coverage distance attainable at 28 GHz for a system with 129 dB maximum measurable path loss (before accounting for antenna gains) and a 5 dB SNR as a function of different TX and RX antenna gains, with PLEs ranging from two to five. It is apparent from the figure that for a specific PLE, the maximum coverage distance grows exponentially with increasing TX-RX antenna gains, indicating that the use of high gain directional steerable antennas along with beam combining and beamforming algorithms will allow for new degrees of freedom in radio link management [1], [43], [44], [57].

### VI. mmWAVE OUTAGE STUDIES

Extensive outage studies are necessary to determine coverage distances and system configurations for mmWave wireless communications networks. Due to the extra attenuation in free space path loss at mmWaves because of the “first meter” loss attributable to the increase in frequency, as well as environmental and rain attenuation, it is predicted that cell radii of several hundred meters will provide favorable coverage with dense base station and UE deployment in urban areas, to reach multi-Gbps speeds [3], [80]. A 200 m cell radius means that the distance between base stations (i.e., inter-site distance) is 400 m. However, it is predicted that 5G mmWave systems will have multiple access points on every street corner in dense UMi environments [3], [10]. Previous work for outage studies at mmWaves, specifically the LMDS band around 28 GHz,

showed poor coverage distance, high signal attenuation, deep fading, and unfavorable multipath conditions for cell radii 300 m or greater [81]. Other work by Seidel and Arnold showed that building obstructions at LMDS frequencies are a major limitation in providing good coverage in a cell [11]. They did show that the LOS component was very strong, but that NLOS conditions were unfavorable. Their limiting view was based on cell sizes that were on the order of several kilometers at the time. With the concept of compact cells due to smaller form factors and newer technologies, more positive assertions can be made from the data given here.

An outage study at 38 GHz conducted in the summer of 2011 on the UTA campus provided probabilities for path loss measurable up to 160 dB [80]. Table X displays the outage probabilities from [80], for coverage distances within 200 m and up to 500 m, for base stations with heights of 18 m and 36 m. The coverage regions for both transmitters are shown in [80, Figs. 2 and 3]. The study revealed that all locations within 200 m of the base station (LOS and NLOS) had detectable signal for a system with 160 dB maximum measurable path loss [35].

An outage study at 28 GHz in downtown Manhattan was first mentioned in [3] and then presented in [82]. Some of the initial results reported in [82] were incorrect, as some outages were computed for distances up to 200 m, and some were computed using all locations with distances up to 425 m. Those numbers are corrected here in Table XI for T-R separation distances up to 200 m, and up to 425 m for the 28 GHz measurement campaign. The 50% outage value in Table XI for KAU includes many locations that would not be used in a practical installation, due to obvious blockage by tall buildings. Using a 90 degree azimuthal coverage zone, the outage was found to be less than 20% for this TX [82]. As described in [82], two transmitters at heights of 7 m and one TX at a height of 17 m, with RX heights of 1.5 m were used to measure outage with maximum measurable path loss of 178 dB for recordable links and acquirable PDPs, with outage probabilities displayed in Table XI. It is important to keep in mind that only three different fixed elevation angles were used at the RX, and only one TX elevation angle was used, meaning that the very “best” elevation angles at the TX and RX were not necessarily found in the 28 GHz campaign (this was done in the 73 GHz campaign). While the 28 GHz measurement locations were chosen arbitrarily, mmWave systems lend themselves to site-specific deployment so that outages can be predicted ahead of deployment. Outage probabilities using data in Table XI were computed to find the probability of an outage  $P_{outage}$ , and the probabilities of LOS, or NLOS link as a function of T-R separation distance, similar to the model presented in [39], where three states are chosen for the statistical model having the form:

$$P_{outage}(d) = \max\left(0, 1 - \exp^{-a_{out}d + b_{out}}\right) \tag{10a}$$

$$P_{LOS}(d) = (1 - P_{outage}(d)) \exp^{-a_{los}d} \tag{10b}$$

$$P_{NLOS}(d) = 1 - P_{outage}(d) - P_{LOS}(d) \tag{10c}$$

where the parameters  $a_{los}$ ,  $a_{out}$ , and  $b_{out}$  are determined by fitting the equations to the empirical data via maximum likelihood estimation. The results are based on 74 unique TX-RX location combinations measured for outage. The form of these equations is similar to those found in [83] and [84]. Fig. 4 shows

TABLE X  
38 GHz OUTAGE PROBABILITIES IN AUSTIN, TEXAS OUT TO 500 m [80]. PL STANDS FOR PATH LOSS (FROM [35], [80])

TX Location	TX Height (m)	RX Height (m)	% Outage (PL>160 dB)	% Outage (PL>150 dB)
TX 1 ENS	36	1.5	18.9% (all $d$ ); 0% ( $d \leq 200$ m)	52.8% (all $d$ ); 27.3% ( $d \leq 200$ m)
TX 2 WRW	18		39.6% (all $d$ ); 0% ( $d \leq 200$ m)	52.8% (all $d$ ); 10% ( $d \leq 200$ m)

TABLE XI  
28 GHz OUTAGE PROBABILITIES IN NEW YORK CITY FOR T-R SEPARATION DISTANCES UNDER 200 m AND FOR ALL T-R SEPARATION DISTANCES UP TO 425 m [82]

TX ID	$h_{TX}$ (m)	$h_{RX}$ (m)	# of RXs	% Outage (PL > 178 dB)
COL1	7	1.5	10 ( $d \leq 200$ m)	20.0%
			25 ( $d \leq 425$ m)	68.0%
COL2	7		9 ( $d \leq 200$ m)	11.1%
			25 ( $d \leq 425$ m)	68.0%
KAU	17		20 ( $d \leq 200$ m)	50.0%
			24 ( $d \leq 425$ m)	58.3%
Overall Outage			39 ( $d \leq 200$ m)	33.3%
			74 ( $d \leq 425$ m)	64.9%

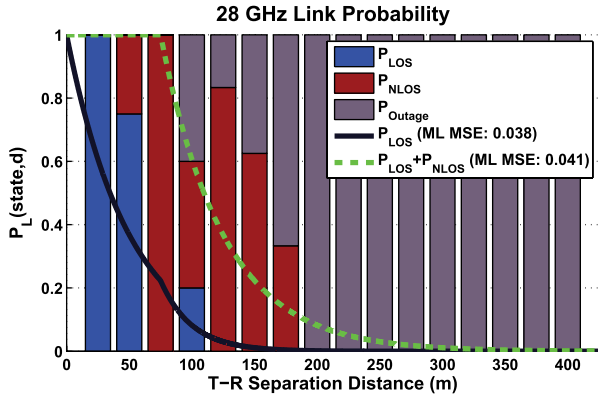


Fig. 4. 28 GHz outage probabilities in New York City for T-R separation distances up to 425 m including measured data and synthesized models [39], [82]. The maximum likelihood mean square error (MSE) is displayed for both fitted curves.

the fractions of outage types for the three observable states in bins of 25 m as well as the probability density functions in Eq. (10) (parameter values are shown in Table XII). Note that Fig. 4 and corresponding values in Table XII differ from those that appear in [39], the result of [39] blending bin widths together for 50 m rather than 25 m. In addition, the outage model in Table XII and Fig. 4 uses an updated database with more TX-RX combinations for outage.

A similar outage study was conducted for the 73 GHz measurement campaign [82], and is updated here. Table XIII displays the outage information for TX height diversity for ranges up to 216 m, as one TX-RX combination tested was farther than 200 m for both mobile and backhaul measurements. Link probability for the 73 GHz campaign was dependent upon observing a signal with 181 dB maximum measurable path loss. Table XIII shows outages for specific transmitters for the mobile and backhaul scenarios in addition to overall outage for the mobile, backhaul, and hybrid scenarios. Fig. 5 displays an outage probability graph for 73 GHz and Table XII shows the estimated parameters, similar to the 28 GHz outage probabilities. The outage results show that mmWave coverage with

TABLE XII  
28 GHz AND 73 GHz OUTAGE PROBABILITY PARAMETERS [39], [83], [84]

Frequency	$1/a_{out}$	$b_{out}$	$1/a_{los}$
28 GHz	50 m	1.8	50 m
73 GHz	45.5 m	3.3	37 m

The 28 GHz measurements used a limited number of fixed elevation pointing angles when compared to the 73 GHz measurements, resulting in more outages at 28 GHz than at 73 GHz. We would expect similar if not slightly less outage probabilities at 28 GHz as compared to 73 GHz, as a function of distance, if identical locations and similar antenna pointing approaches were used at both frequencies.

high gain directional antennas is sufficient for distances up to 200 m for a Manhattan environment in which the 28 and 73 GHz measurements were conducted.

Using the 28 and 73 GHz measurements from this paper as a test case, a novel site-specific ray tracing method given in [93] was shown to provide excellent prediction for the LOS and NLOS probabilities, offering a better fit than (10). Raw data for 28, 38 and 73 GHz omnidirectional path loss that includes outage information are found in [94].

## VII. MULTIPATH COMPONENTS AND RMS DELAY SPREAD AT MmWAVE

### A. Multipath Effect

In the early days of wireless communications, multipath was considered a negative aspect of the propagation channel due to intersymbol interference (ISI). However, researchers over time have developed algorithms and systems to take advantage of multipath. MmWave systems in NLOS dense urban environments will use beam combining and beamforming techniques, as described in Section V, to exploit multipath fading in the environment, in perhaps different ways than current 4G/LTE systems do [49]. Numerous antenna elements at the RX will be used to increase the received SNR or reduce interference

TABLE XIII  
73 GHz OUTAGE PROBABILITIES IN NEW YORK CITY FOR T-R SEPARATION DISTANCES UP TO 200 m AND OVER ALL DISTANCES MEASURED FOR MOBILE ( $h_{RX} = 2$  m), BACKHAUL ( $h_{RX} = 4.06$  m), AND HYBRID (MOBILE + BACKHAUL) SCENARIOS [82]

TX ID	$h_{TX}$ (m)	$h_{RX}$ (m)	# of RXs	% Outage (PL > 178 dB)
COL1	7	2	11 ( $d \leq 200$ m)	27.3%
			11 ( $d \leq 216$ m)	27.3%
COL2	8 ( $d \leq 200$ m)		25.0%	
	9 ( $d \leq 216$ m)		33.3%	
KAU	17		11 ( $d \leq 200$ m)	0.0%
			11 ( $d \leq 216$ m)	0.0%
KIM1	7		3 ( $d \leq 200$ m)	0.0%
			3 ( $d \leq 216$ m)	0.0%
KIM2	7		2 ( $d \leq 200$ m)	0.0%
			2 ( $d \leq 216$ m)	0.0%
<b>Overall Mobile Outage</b>			35 ( $d \leq 200$ m)	14.3%
			36 ( $d \leq 216$ m)	16.7%
COL1	7	4.06	7 ( $d \leq 200$ m)	42.9%
			7 ( $d \leq 216$ m)	42.9%
COL2	13 ( $d \leq 200$ m)		15.4%	
	14 ( $d \leq 216$ m)		21.4%	
KAU	17		11 ( $d \leq 200$ m)	0.0%
			11 ( $d \leq 216$ m)	0.0%
KIM1	7		3 ( $d \leq 200$ m)	0.0%
			3 ( $d \leq 216$ m)	0.0%
KIM2	7		3 ( $d \leq 200$ m)	0.0%
			3 ( $d \leq 216$ m)	0.0%
<b>Overall Backhaul Outage</b>			37 ( $d \leq 200$ m)	13.5%
			38 ( $d \leq 216$ m)	15.8%
<b>Overall Hybrid Outage</b>			72 ( $d \leq 200$ m)	13.9%
			74 ( $d \leq 216$ m)	16.2%

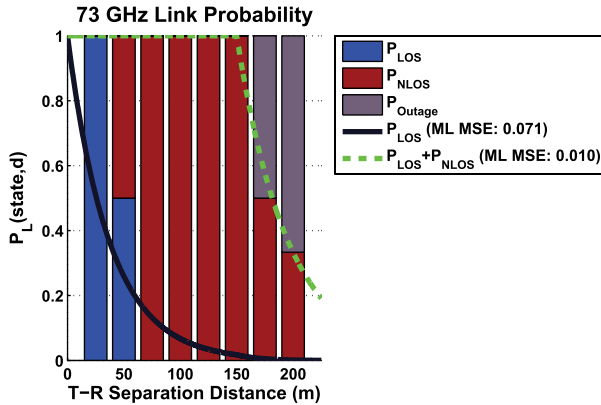


Fig. 5. 73 GHz outage probabilities for the hybrid scenario in New York City for T-R separation distances up to 216 m [39], [82]. The maximum likelihood mean square error (MSE) is displayed for both fitted curves.

via beam combining or beamforming techniques, by combining multipath from many AOA and excess delays [49]. It is expected that tens to hundreds of miniature on-chip electrically steerable antennas will be used in mmWave devices to find the strongest multipath AOA at the RX for improving SNR, and to extend coverage distances [78].

The maximum and average number of resolvable MPCs at arbitrary antenna azimuth and elevation pointing angles as a function of T-R separation distance for the 28 GHz narrow-beam measurements in Manhattan in a NLOS environment are displayed in Fig. 6. The maximum and average number of resolvable MPCs at arbitrary antenna azimuth and elevation

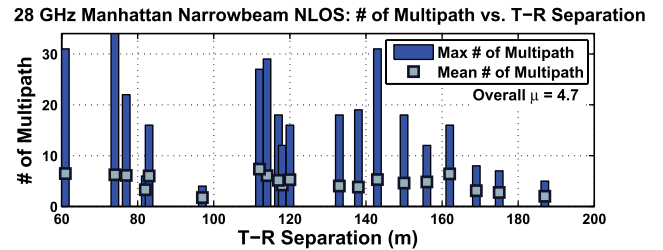


Fig. 6. 28 GHz unique antenna azimuth and elevation pointing angle NLOS maximum and mean MPCs as a function of T-R separation distance for narrowbeam antenna measurements in Manhattan. The overall mean number of MPCs over all TX-RX antenna pointing angle combinations and T-R separation distances is also presented.

pointing angles as a function of T-R separation distance for 73 GHz base station-to-mobile access and backhaul measurements in a NLOS scenario are displayed in Fig. 7.

A peak-finding algorithm rather than a binning technique was used to determine the number of MPCs in each PDP at both 28 GHz and 73 GHz. For the 28 GHz measurements, the average number of MPCs follows a uniform trend over all T-R separation distances with a mean value of 4.7 over all unique pointing angles and distances. At 73 GHz, the average number of MPCs detected at any unique pointing angle for NLOS is generally uniform for both access and backhaul measurements, and the mean value over all unique pointing angles and distances is 3.3 and 2.9 for access and backhaul, respectively. Because the mobile RX is lower to the ground, the signal may encounter more ground reflections. When rounding, there are on average three resolvable MPCs detectable for any

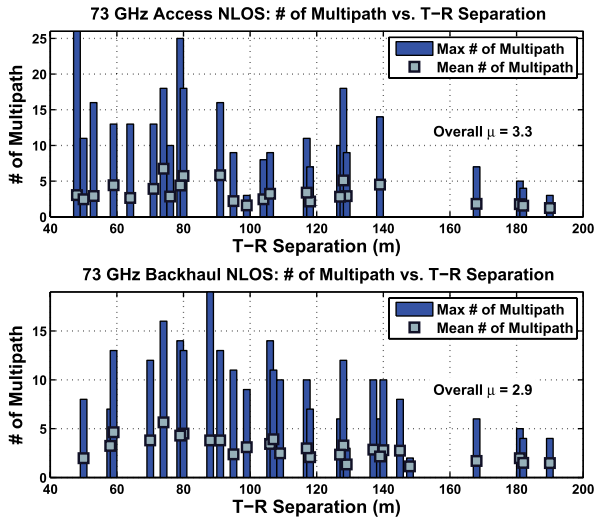


Fig. 7. 73 GHz unique antenna azimuth and elevation pointing angle NLOS maximum and mean MPCs as a function of T-R separation distance for narrowbeam antenna access and backhaul measurements. The overall mean number of MPCs over all TX-RX antenna pointing angle combinations and T-R separation distances is also presented.

unique antenna pointing angle combination between the TX and RX at 73 GHz in a NLOS environment.

Overall, there are more resolvable MPCs as a function of T-R separation distance in NLOS environments at 28 GHz compared to 73 GHz, attributed to stronger signals (less free space loss in the first meter) and the larger wavelengths at 28 GHz, which allow the signal to reflect more and scatter less. The 73 GHz signals have a smaller wavelength and a higher possibility of getting caught in tiny building cracks and rough surfaces, leading to diffusion. Another key observation is that for both the 28 and 73 GHz measurements, the maximum number of NLOS MPCs detected at an arbitrary pointing angle combination between the RX and TX decreases with distance. This does not necessarily mean that there is less multipath at farther T-R separation distances; this observation is more likely attributed to the noise floor of our detection system since MPCs become weaker as the T-R separation distance or propagation path distance increases.

*B. RMS Delay Spread with Directional Antennas*

RMS delay spread is an important characteristic of a radio propagation channel [85]. The RMS delay spread values presented here are for LOS environments at 28 and 73 GHz, in addition to NLOS environments at 28, 38, and 73 GHz. Measurements across all three bands consistently show that when directional antennas are used, the LOS channel provides virtually no delay spread (the RMS delay spread is the width of the channel sounder’s impulse response). This is clear from Fig. 11 (below) [41], [49]; however, if antenna beams are not aligned on boresight in LOS environments, RMS delay spreads much greater than 50 ns can occur [13], [72]. For the narrowbeam (Manhattan) and widebeam (Brooklyn) 28 GHz measurements, the RMS delay spread cumulative distribution functions (CDFs) follow similar trends. From Fig. 8, it is apparent that 90% of the RMS delay spreads were below 50 ns for both narrowbeam and widebeam measurements, with the widebeam antenna providing slightly more delay

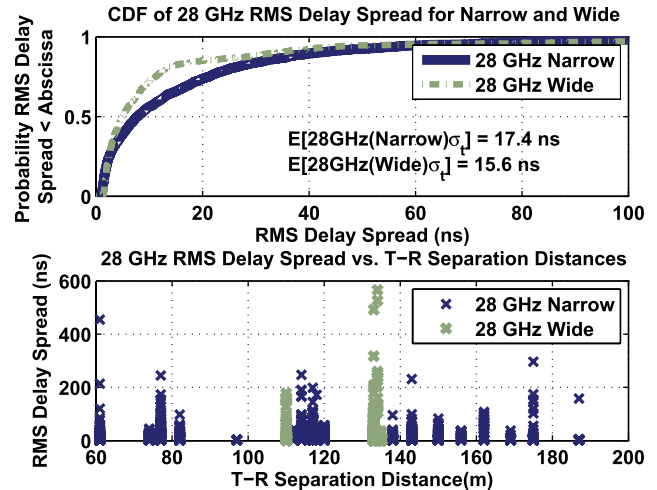


Fig. 8. 28 GHz NLOS directional RMS delay spread CDFs and as a function of T-R separation distance for narrowbeam (Manhattan) and widebeam (Brooklyn) antenna measurements.

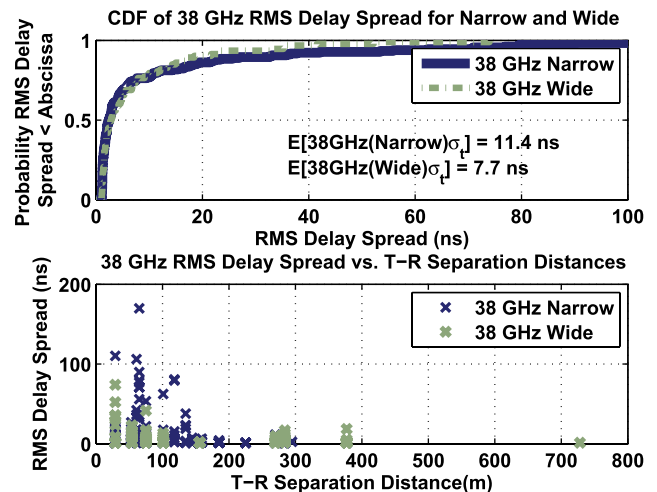


Fig. 9. 38 GHz NLOS directional RMS delay spread CDFs and as a function of T-R separation distance for narrowbeam and widebeam antenna measurements in Austin.

spreads below 40 ns, and with a larger mean delay spread of 17.4 ns for narrowbeam in Manhattan, compared to 15.6 ns for widebeam in Brooklyn. The slightly larger mean RMS delay spread for narrowbeam measurements can be attributed to the tail behavior of larger values due to the larger dynamic range of our 28 GHz channel sounder system with higher gain antennas compared to the reduced path loss measurement range using a widebeam TX antenna in Brooklyn. Fig. 8 also displays the RMS delay spreads as a function of T-R separation distance, and is distributed relatively uniformly across all distances for narrowbeam measurements.

Fig. 9 shows the RMS delay spread CDF for the 38 GHz narrowbeam and widebeam measurements. For 38 GHz, it is apparent that 90% of the RMS delay spreads are below 40 ns for both narrowbeam and widebeam measurements, similar to 28 GHz measurements. In addition, the mean RMS delay spread is 11.4 ns for narrowbeam and 7.7 ns for widebeam measurements. The RMS delay spread as a function of T-R separation distance follows a decreasing trend as the T-R

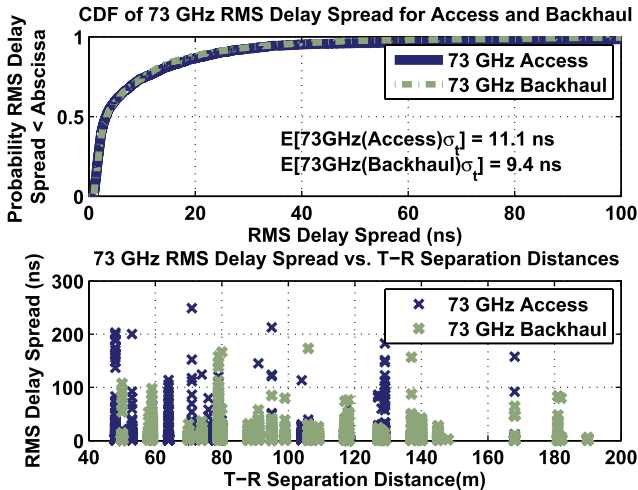


Fig. 10. 73 GHz NLOS directional RMS delay spread CDFs and as a function of T-R separation distance for narrowbeam antenna access and backhaul measurements in Manhattan.

separation distance increases. This is expected in a less cluttered environment like Austin since the farther the separation distance, the more the signal will be attenuated in the absence of large scatterers, thus falling below the detectable range of the system.

Fig. 10 shows the RMS delay spread for the access and backhaul scenarios at 73 GHz for the NLOS unique pointing angle scenario. The trend here shows that a majority of the RMS delay spreads are below 25 ns for unique pointing angle measurements. The access measurements have a slightly larger mean RMS delay spread, and this can be attributed to more reflected paths reaching the RX at a lower height, as compared to backhaul RX antenna heights. Similar to the 28 GHz and 38 GHz bands, at 73 GHz it is apparent that the RMS delay spread decreases as the T-R separation distance increases, but the urban New York City measurements do not decrease as rapidly, due to the scattering and reflections from large buildings.

The mean RMS delay spreads at 38 and 73 GHz are smaller than at 28 GHz, due to the more reflective environment of Manhattan and greater energy being scattered at lower mmWave frequencies (where the first meter of free space path loss is lower). Wavelengths at 73 GHz are smaller than at 28 and 38 GHz, giving rise to more diffuse scattering during propagation which results in weaker paths not detectable at the RX. A normalized mean square error (NMSE) [90] method is employed to fit a simple exponential model to the distribution of measured RMS delay spread values at 28, 38, and 73 GHz, by setting the empirical mean RMS delay spread values (from the CDFs of measured data) equal to the mean of the exponential model. The distribution parameters and goodness of fit (GOF) are given in Tables XIV, XV, and XVI, where the NMSE GOF measure ranges from  $-\infty$  to 1, where  $-\infty$  indicates a poor fit, and 1 indicates a perfect fit. It can be seen that the range of RMS delay spread values are reasonably well modeled by a simple exponential distribution.

RMS delay spread and maximum excess delay (MED) spreads from PDPs may be useful for designing mmWave

TABLE XIV  
28 GHz RMS DELAY SPREAD DISTRIBUTION FIT AND GOODNESS OF FIT VIA NMSE

28 GHz (10.9° Az. HPBW RX) RMS Delay Spread Goodness of Fit		
Location	Distribution	GOF
Manhattan (10.9° Az. HPBW TX)	exponential ( $\mu = 17.4 \text{ ns}$ )	0.60
Brooklyn (28.8° Az. HPBW TX)	exponential ( $\mu = 15.6 \text{ ns}$ )	0.35

TABLE XV  
38 GHz RMS DELAY SPREAD DISTRIBUTION FIT AND GOODNESS OF FIT VIA NMSE

38 GHz (7.8° Az. HPBW TX) RMS Delay Spread Goodness of Fit		
RX Antenna	Distribution	GOF
Narrowbeam (7.8° Az. HPBW)	exponential ( $\mu = 11.4 \text{ ns}$ )	0.40
Widebeam (49.4° Az. HPBW)	exponential ( $\mu = 7.7 \text{ ns}$ )	0.83

TABLE XVI  
73 GHz RMS DELAY SPREAD DISTRIBUTION FIT AND GOODNESS OF FIT VIA NMSE

73 GHz (7° Az. HPBW TX & RX) RMS Delay Spread Goodness of Fit		
Scenario	Distribution	GOF
Access	exponential ( $\mu = 11.1 \text{ ns}$ )	0.46
Backhaul	exponential ( $\mu = 9.4 \text{ ns}$ )	0.57

directional systems that rely on beam searching algorithms. Temporal statistics for the best unique antenna pointing directions at the TX and RX in the elevation and azimuth planes that result in the lowest path loss may be useful for standards contributions. For both the 28 and 73 GHz bands, RMS delay spread, MED 10 dB down from the maximum peak, and MED 20 dB down from the maximum peak were determined for the TX-RX beams that resulted in the lowest path loss over all locations, and are displayed in Table XVII, with comprehensive tables for each TX-RX location combination given in [49].

Fig. 11 shows the RMS delay spread CDFs for the single strongest PDP for each TX-RX location combination for the 28 and 73 GHz access measurements<sup>¶</sup> [41]. Both 28 and 73 GHz LOS measurements show that a majority of the RMS delay spreads are below 2 ns. In NLOS environments, 90% of the RMS delay spreads are below 60 ns and 20 ns when considering the unique antenna pointing angle with the strongest received power for the 28 GHz narrowbeam and 73 GHz mobile measurements, respectively. The 73 GHz backhaul measurements follow the same trend in LOS and NLOS environments as the 73 GHz mobile measurements. From Table XVII we can see that the minimum RMS delay spread, MED 10 dB, and MED 20 dB for the LOS environment are comparable at both 28 and 73 GHz and their various scenarios. The same holds true for the minimum NLOS values for each band and the various scenarios. The values presented in Table XVII provide insight for systems that systematically search for the strongest TX and RX antenna pointing angles that result in low RMS delay spreads (so that simple equalization methods may be used). The temporal statistics for these strong

<sup>¶</sup>Five locations were used for the 28 GHz statistics as the sixth LOS location had a larger than normal RMS delay spread (153.5 ns) since the TX and RX antennas were not properly aligned on boresight for that T-R separation distance.

TABLE XVII  
 THE MINIMUM, MAXIMUM, AND MEAN RMS DELAY SPREAD, MED 10 dB DOWN FROM THE MAXIMUM PEAK, AND MED 20 dB DOWN FROM THE MAXIMUM PEAK, FOR THE DIRECTIONAL BEAMS WITH THE LOWEST PATH LOSS FROM THE 28 AND 73 GHz MEASUREMENTS. MED 10 dB REFERS TO MAXIMUM EXCESS DELAY 10 dB DOWN FROM THE MAXIMUM PEAK, AND MED 20 dB REFERS TO MAXIMUM EXCESS DELAY 20 dB DOWN FROM THE MAXIMUM PEAK

Delay Spreads for Directional Beams with Lowest Path Loss										
Environment		LOS								
		RMS Delay Spread (ns)			MED 10 dB (ns)			MED 20 dB (ns)		
Freq.	Scenario	min	max	mean	min	max	mean	min	max	mean
28 GHz	Narrowbeam	0.83	153.6	0.85 <sup>†</sup>	4.4	362.9	76.1	5.0	405.7	85.3
73 GHz	Access	0.81	1.7	1.2	4.3	25.1	12.4	4.9	25.8	13.8
73 GHz	Backhaul	0.93	1.9	1.5	4.6	24.7	19.5	7.6	28.2	22.6
Environment		NLOS								
		RMS Delay Spread (ns)			MED 10 dB (ns)			MED 20 dB (ns)		
Freq.	Scenario	min	max	mean	min	max	mean	min	max	mean
28 GHz	Narrowbeam	0.96	165.1	25.7	5.1	221.3	53.7	6.3	1384.8	152.2
28 GHz	Widebeam	1.4	20.0	7.1	5.4	18.6	8.9	11	171.6	56
73 GHz	Access	0.92	30.3	7.1	4.3	95.2	27.1	5.5	159.1	39.1
73 GHz	Backhaul	0.92	48.5	5.6	4.4	169.6	22.6	4.9	171.3	30.7

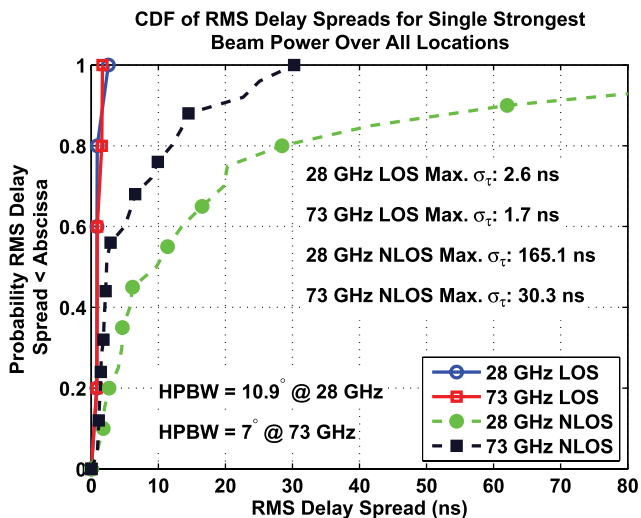


Fig. 11. 28 GHz and 73 GHz Access CDFs of RMS delay spreads for the single strongest received power for each TX-RX location combination that resulted in the lowest path loss in LOS and NLOS environments [41].

directional beams may help define the channel matrix used to describe the LOS and NLOS mmWave channels.

VIII. SPATIAL STATISTICS FOR MmWAVE CHANNELS

A. Spatial Lobes

MmWave transmissions will be very directional as a result of the high-gain antennas needed at the base station and mobile handset to make up for the increased free space path loss, a major shift from today’s fixed sectorized cells and omnidirectional receivers. Our 28 GHz and 73 GHz measurements have revealed that energy tends to depart and arrive at a few principal AOD and AOA spatial lobes, where we define a spatial lobe to represent a main direction of arrival (departure) at which groups of traveling MPCs arrive (depart) over a contiguous range of angles in azimuth and elevation over several hundreds of nanoseconds. Spatial lobes model the phenomenon of spatial directionality in mmWave channel characterization, and have been used successfully to model the 2-D and 3-D spatial channels at 28 GHz based on our field measurements [3], [13], [45], [46], [62], [65].

3GPP and WINNER II channel models represent spatial clusters of MPCs by assigning one group of traveling MPCs to one random AOA. We have observed from field measurements that multiple groups of multipath clusters can arrive at the same unique pointing angle in azimuth and elevation but at different time delays, and we therefore generalize spatial clusters into spatial lobes, where a spatial lobe can receive more than one traveling cluster. This observation was possible due to the measurement system of Table I that enables 2.5 ns MPC resolution and highly directional channel measurements, thus enabling the detection of clusters of MPCs over several hundreds of nanoseconds in excess delay.

Channel characterization of the impulse response has thus far focused on modeling the time domain, the AOA in the azimuth plane [86], [87], and/or the AOA and AOD in the azimuth and elevation planes [76], [88], to account for directionality at the TX and RX. We generalize this by introducing directionality at the TX and RX, in both the azimuth and elevation planes, by extracting spatial lobe statistics from field measurements. Spatial lobe statistics are easily extracted from 3-D power spectra by defining a power threshold, where all contiguous power levels above such a threshold belong to one 3-D spatial lobe [45], [46], [62]. This spatial thresholding technique allows us to extract RMS lobe angular spreads, a new statistic that quantifies directional spreads at the TX and RX.

Directional spatial statistics can be used to model spatial directionality at both the TX and RX. Table XVIII shows the 3-D RMS lobe angular spreads extracted from our 28 GHz and 73 GHz field measurements, in both LOS and NLOS environments (where 3-D RMS lobe angular spread is defined in [46]), using a -10 dB lobe threshold. Field measurements provided enough data to separate the NLOS scenarios by different frequencies, while the LOS measurements were too few (only three locations at 28 GHz, and six locations at 73 GHz), motivating us to pool measured data from both frequencies to find statistics (e.g. model parameters) for a joint frequency scenario. The LOS RMS lobe azimuth spreads are on average slightly larger than the NLOS RMS lobe azimuth spreads, indicating that energy arrives in narrow lobes at the RX, while being more distributed over space and stronger in LOS environments (see Figs. 17 and 18). In NLOS environments, the 28 GHz 3-D lobe

TABLE XVIII  
SUMMARY OF 3-D SPATIAL LOBE STATISTICS FOR JOINT 28 GHz AND 73 GHz LOS, 28 GHz NLOS, AND 73 GHz ACCESS NLOS ENVIRONMENTS, OBTAINED USING A -10 dB LOBE THRESHOLD [46]

Frequency Scenario	LOS	NLOS	
	Joint 28-73 GHz	28 GHz	73 GHz
AOA RMS Lobe Azimuth Spread ( $\mu$ [°], $\sigma$ [°])	(7.0, 4.2)	(6.8, 4.8)	(3.7, 2.3)
AOA RMS Lobe Elevation Spread ( $\mu$ [°], $\sigma$ [°])	(7.0, 4.7)	(6.7, 2.3)	(2.2, 1.7)

TABLE XIX  
38 AND 60 GHz P2P CLOSE-IN FREE SPACE REFERENCE DISTANCE ( $d_0 = 1$  m) DIRECTIONAL PATH LOSS MODELS. PLE IS THE PATH LOSS EXPONENT,  $\sigma$  IS THE STANDARD DEVIATION OF THE ZERO-MEAN GAUSSIAN RANDOM VARIABLE (SHADOW FACTOR) ABOUT THE MMSE LINE. 60 GHz VEHICULAR MODELS ARE ALSO PRESENTED

P2P Directional Path Loss Models ( $d_0 = 1$ m)								
			LOS		NLOS		NLOS-best	
Frequency	TX Height (m)	RX Height (m)	PLE	$\sigma$ [dB]	PLE	$\sigma$ [dB]	PLE	$\sigma$ [dB]
38 GHz	1.5	1.5	2.0	3.8	3.9	10.6	3.3	7.7
60 GHz			2.2	2.0	3.6	9.0	3.3	9.2
Vehicular Directional Path Loss Models ( $d_0 = 1$ m)								
			LOS		NLOS		NLOS-best	
Frequency	TX Height (m)	RX Height (m)	PLE	$\sigma$ [dB]	PLE	$\sigma$ [dB]	PLE	$\sigma$ [dB]
60 GHz	1.5	1.5	2.5	3.5	5.4	14.8	5.0	10.9

azimuth spreads are larger than at 73 GHz, indicating that 28 GHz propagation is more spatially prominent than at 73 GHz, i.e., stronger energy comes from a larger number of angles at lower mmWave frequencies. The 73 GHz measurement system uses an increased overall measurement range to offset some additional free space loss as compared to the 28 GHz system (see Table I), hence the smaller angular spreads at 73 GHz may be due to the narrower TX antenna, as well as to increased environmental scattering that dampens energy over a wider field of view.

IX. PEER-TO-PEER AND VEHICULAR CHANNEL RESPONSES

Wideband P2P measurements as described in [34] were conducted at UTA along a pedestrian walkway surrounded by buildings at both 38 and 60 GHz, over T-R separation distances ranging from 19 to 129 meters. Similar to the directional path loss models presented for base station-to-mobile (access) and base station-to-base station (backhaul) scenarios described in Section III, directional path loss models with respect to a 1 m close-in free space reference distance are presented in Table XIX. The LOS boresight-to-boresight measurements yielded measured PLEs and shadow factors of 2.0 and 3.8 dB, and 2.2 and 2.0 dB, at 38 GHz and 60 GHz, respectively, indicating a relatively good fit to free space propagation ( $n = 2$ ) with small large-scale signal fluctuations resulting most likely from coherent combining of the direct LOS path and ground-bounces. The NLOS measurements showed increased signal attenuation over distance, with measured PLEs and shadow factors of 3.9 and 10.6 dB, and 3.6 and 9.0 dB, at 38 GHz and 60 GHz, respectively, resulting from random signal level fluctuations caused by large scatterers such as building surfaces and trees. The slight increase of the LOS PLE at 60 GHz, above free space, is expected due to increased oxygen absorption [34], [61]. When selecting the strongest beam at each measured TX-RX location, the specific increases in link margin over distance are 6 dB/decade and 3 dB/decade at 38 GHz and 60 GHz, respectively.

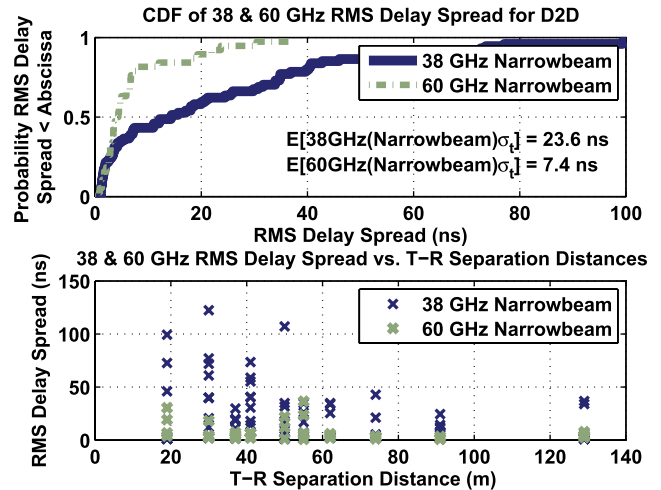


Fig. 12. 38 and 60 GHz directional antenna P2P RMS delay spread CDF and as a function of T-R separation distance.

TABLE XX  
38 GHz AND 60 GHz P2P RMS DELAY SPREAD DISTRIBUTION FIT AND GOODNESS OF FIT VIA NMSE

P2P RMS Delay Spread Goodness of Fit		
Frequency	Distribution	GOF
38 GHz (7.8° Az. HPBW TX & RX)	Exp ( $\mu = 23.6$ ns)	0.67
60 GHz (7.3° Az. HPBW TX & RX)	Exp ( $\mu = 7.4$ ns)	0.76

Fig. 12 shows the P2P RMS delay spread CDFs and RMS delay spreads as a function of T-R separation distances, obtained from the 38 GHz and 60 GHz P2P measurements. The 60 GHz RMS delay spreads are much lower than the 38 GHz RMS delay spreads. This can be accounted for with two explanations. First, the 60 GHz transmit power was only 5 dBm whereas the 38 GHz transmit power was 22.1 dBm, thus weaker components that the 38 GHz system detected were not able to be detected by the 60 GHz system. Second, air attenuation at 60 GHz is much greater than at 38 GHz and scattering is also more diffuse, resulting in less detectable energy. Table XX shows the exponential distributions that were fit to

the empirical RMS delay spread values from the P2P measurements at 38 GHz and 60 GHz. The mean values of the empirical RMS delay spread CDFs were used to generate exponential distribution models using the NSME method, and the corresponding GOF measures between the modeled and empirical distributions are given in Table XX at both 38 GHz and 60 GHz.

The mean value of the RMS delay spreads for all vehicular measurements was 2.7 ns. Overall, the results are favorable for short-range communications in a vehicle-to-vehicle or in-vehicle mmWave system. The NLOS PLE of 5.4 (see Table XIX) is rather high for the 60 GHz vehicular scenario as the signal attenuates by 54 dB/decade of distance, due to signal blockage of other vehicles and within the vehicle, and increased oxygen absorption, but short range communications such as P2P and vehicular to vehicular (V2V), will be able to withstand such loss.

X. 28 GHz mmWAVE WIDEBAND CHANNEL STATISTICS

The 28 GHz propagation measurements were used to create a 3-D statistical channel impulse response model capable of generating omnidirectional PDPs and 3-D power spectra at the transmitter and receiver, which recreated the statistics of the measured channels [45], [46]. Previous work considered 2-D channel models, which have been reported in [1], [45], [46], and were used for mmWave system-wide simulations and capacity analyses in a MIMO system, showing that multiple beams can be exploited to achieve significant spatial multiplexing and beamforming gains from MPCs departing from multiple distinct directions at the base station [49].

Among the many results discovered, it is worth mentioning that energy was observed to arrive at distinct *spatial lobes* [45]. Field measurements revealed that MPCs not only travel close together in space and time, but can also arrive at the receiver at much larger delays than previously considered in current UHF/Microwave channel models, when taking high-gain directional horn antennas into account.

The widespread 3GPP and WINNER II channel models do not distinguish a spatial cluster from a time cluster. In our model, we introduce concepts of time clusters and spatial lobes, where a spatial lobe can receive multiple time clusters, as observed from field measurements with high-gain antennas. Intra-cluster statistics revealed that time clusters are subdivided into smaller microscopic subpath components, whose power levels exhibited (on average) an exponential fall-off behavior as shown in Fig. 16. This phenomenon was found in both LOS and NLOS environments as displayed in Figs. 13 and 14 at unique pointing angles. Fig. 14 illustrates cluster subpaths as measured from a unique RX antenna pointing angle. Five distinct time clusters and intra-cluster subpaths can be observed occurring at discrete excess time delays.

Fig. 15 shows a PDP obtained at a unique azimuth and elevation pointing angle combination, clearly showing two groups of MPCs arriving at excess delays of 0 ns and 360 ns, with the two time clusters composed of multiple intra-cluster subpaths. It is worth mentioning that previous published work used intra-cluster subpaths to successfully model the indoor multipath channel [86], [87], [89]. In our work, a group of MPCs traveling close in time and space are referred to as a

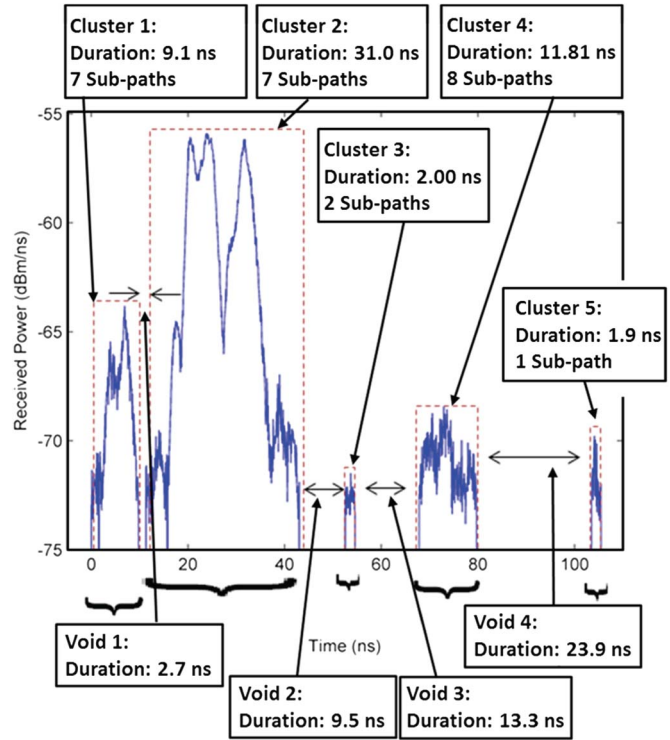


Fig. 13. Typical power delay profile measured at a unique antenna pointing angle. Five distinct time clusters with different cluster time durations are observed, ranging from 9.1 ns to 31 ns. Each time cluster is composed of intra-cluster subpath components occurring within each cluster at discrete time delays [45], [46].

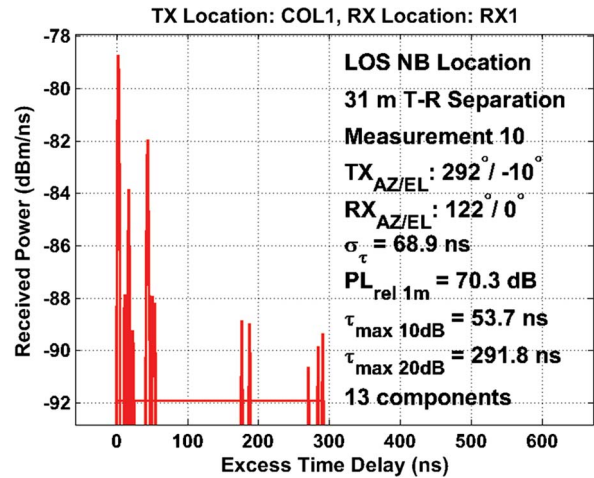


Fig. 14. Typical power delay profile measured at a unique pointing angle in a LOS environment for a T-R separation distance of 31 m. In this PDP, multiple time clusters and intra-cluster subpaths are observed.

*time cluster*, or temporal cluster [45]. Time statistics were extracted by defining a minimum inter-cluster void interval of 25 ns, and subsequently counting the number of time clusters, the number of intra-cluster subpaths, and extracting cluster and subpath power levels in synthesized 3-D omnidirectional PDPs [45], [46]. This simple clustering scheme can resolve multipath channel dynamics in great detail within the smallest multipath time resolution offered by the 3GPP and WINNER models (20 ns) [50] [76], and is easily adjustable to resolve temporal statistics over arbitrary time resolutions using a different minimum inter-cluster void interval. Multipath components

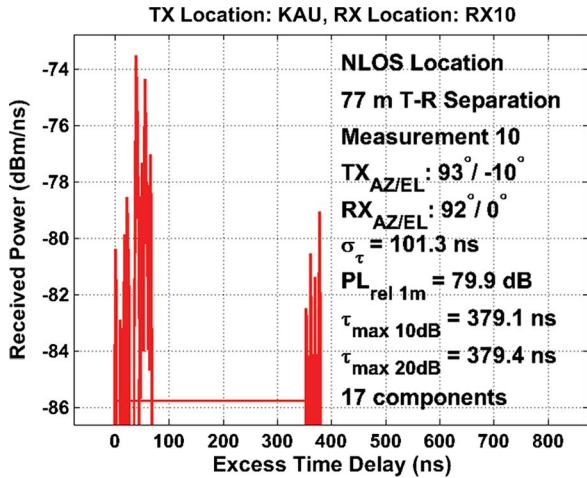


Fig. 15. Typical power delay profile measured at a unique pointing angle in a NLOS environment for a T-R separation distance of 77 m. In this PDP, two time clusters and many intra-cluster subpaths are observed.

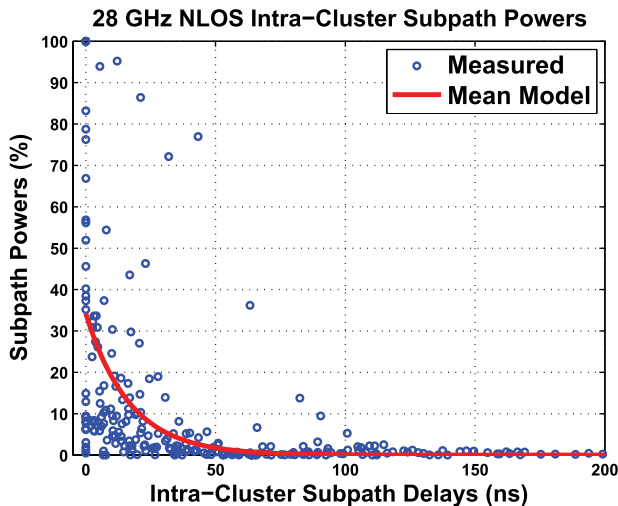


Fig. 16. Intra-cluster subpath power levels (normalized to cluster powers) as a function of intra-cluster subpath delay obtained from the 28 GHz synthesized omnidirectional PDPs in NLOS, extracted using a 25 ns minimum inter-cluster void interval. The power levels are observed to fall-off exponentially. Random fluctuations in power levels may be added using a lognormal random variable with  $\sigma = 6$  dB [46].

tend to arrive at the receiver at many different time delays and angular directions (a result of walkways and streets between buildings, that have typical spatial dimensions of 8 m—roughly 25 ns in propagation delay) in the dense urban propagation environment). The inter-cluster void interval is adjustable and may differ depending on city street layout dimensions. The clustering approach provided models for the time cluster and intra-cluster subpath power levels, yielding an accurate fit to the empirical omnidirectional RMS delay spreads over a large ensemble of simulated PDPs. Note that our previous work considered a 2.5 ns minimum inter-cluster void interval when considering synthesized omnidirectional PDPs in 2-D [45]. We subsequently found this was too small of a value to obtain accurate RMS delay spread tail behavior in monte carlo simulations. Spatial lobe statistics were extracted by applying a  $-10$  dB threshold with respect to the maximum received power angular segment in the 3-D power spectrum [46], while a  $-20$  dB power threshold was used in [45]. We found a

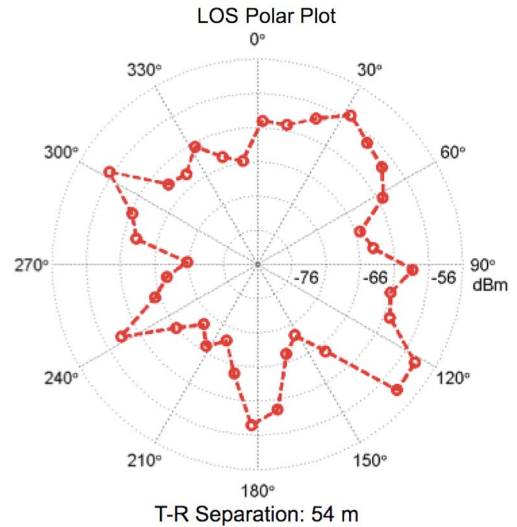


Fig. 17. 28 GHz LOS polar plot for a T-R separation distance of 54 m showing that energy arrives in all measured directions within a 10 dB dynamic range.

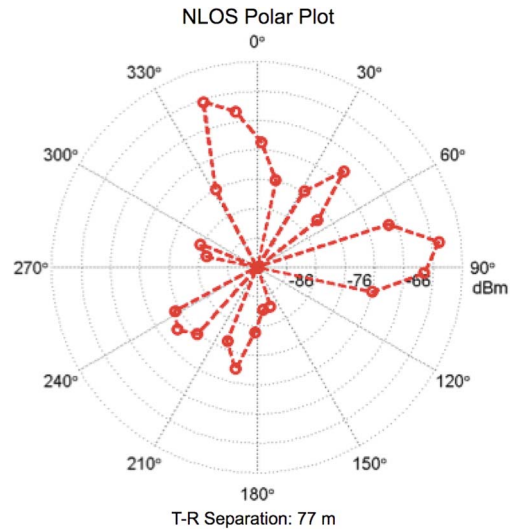


Fig. 18. 28 GHz NLOS polar plot for a T-R separation distance of 77 m showing that energy arrives at distinct AOAs, motivating the use of beamforming and beam combining in mmWave MIMO systems.

$-10$  dB threshold in space is more meaningful for keeping the salient features of a model built from a vast amount of measured data. In our work, we de-coupled time and space by extracting temporal and spatial statistics independently, and then assigned time clusters in a random manner to spatial lobes in order to re-couple the time and space dimensions to produce an accurate joint spatial-temporal channel model (see Step 12 in [46]).

Our 3-D stochastic channel models follow from the 3GPP and WINNER II models, and include simple extensions to account for intra-cluster delays and power levels (based on our field data), and also provide a detailed methodology for generating segmented AOD and AOA power spectra with a  $1^\circ$  resolution in the azimuth and elevation planes. Accurate reproduction of measured channel PDPs and a complete step-by-step procedure for generating mmWave omnidirectional PDPs and power spectra has been presented in [46].

There are significant differences in the spatial properties of LOS and NLOS mmWave channels. Figs. 17 and 18 show

two typical polar plots obtained from measurements in a LOS and NLOS environment, respectively, where each ‘dot’ corresponds to the total received power (area under the PDP) at each measured unique pointing angle in azimuth, and at an elevation of  $0^\circ$  (parallel to the horizon). The contrast in spatial power variation encountered in LOS environments as compared to NLOS environments as displayed in Figs. 17 and 18 is significant, indicating a great deal of azimuthal sparsity of energy and more sharply defined AOAs in NLOS environments.

## XI. CONCLUSION

This paper presents the first combined contribution of wideband mmWave outdoor propagation measurements and channel models at 28, 38, 60, and 73 GHz for base station-to-mobile (access), base station-to-base station (backhaul), peer-to-peer, and vehicular (V2V) scenarios. The measurement results include channel characteristics such as path loss models for each frequency, multipath delay spread, number of multipath components, outage probabilities, and initial mmWave statistical spatial channel model (SSCM) statistics. In general, path loss exponents are larger in New York City than in Austin due to the highly populated urban environment of the former, but are not markedly different from today’s UHF cellular systems. Directional and omnidirectional path loss models were both presented with respect to a 1 m close-in free space reference distance. Using a close-in reference distance path loss model is advantageous because of the standard use, the frequency dependence, and the ease by which measurements across different bands and scenarios may be compared, whereas the *alpha-beta* model is only sufficient across the specific measurement range and is difficult to use for comparison at different frequencies or environments. The omnidirectional PLE ranges from 1.8 to 2.1, and from 2.4 to 3.5 in LOS and NLOS environments, respectively, at 28, 38, and 73 GHz, not much different than today’s UHF/Microwave path loss models. The measurements and models provided here suggest that PLE tends to increase slightly with an increase in frequency for a given environment, due to the diffuse scattering of signals with smaller wavelengths. The close-in reference distance path loss models allow comparisons using the Distance Extension Exponent (DEE) and Distance Extension Factor (DEF) for either increasing SNR or extending coverage distance when combining beams with the strongest received powers. Coherently combining the four best measured beams at both 28 and 73 GHz has shown that coverage distance can be extended by more than a factor of 2.

Multipath has proven to be advantageous in increasing SNR and signal strength in current 4G/LTE systems, but it is still up for debate whether mmWave systems will employ the same algorithms and technologies. The average number of resolvable MPCs in any arbitrary antenna pointing direction is larger at 28 GHz (4.7) than 73 GHz (3.3) in NLOS environments for the base station-to-access scenario, likely due to the larger wavelength and more pronounced reflected and scattered energy at 28 GHz. The average NLOS RMS delay spread for 28, 38, and 73 GHz is 17.4, 11.4, and 11.1 ns, respectively, using arbitrarily pointed narrowbeam antennas in the base station-to-access sce-

nario, and decreases when widebeam antennas are used. The mean NLOS RMS delay spreads below 20 ns compare well with previous outdoor measurements at 60 GHz [28]. RMS delay spread is generally inversely proportional to the T-R separation distance in less urban environments such as Austin, and is much larger in New York City than in Austin, because of the highly reflective dense urban environment. We have also shown that the single strongest directional link between the TX and RX in dense urban environments often results in the link with low RMS delay spread, and this knowledge will be important for future mmWave systems that will be highly directional with numerous antenna elements. The outage studies show better coverage at 38 GHz in Austin than in New York City at 28 GHz and 73 GHz, since New York City is a dense urban environment with tall buildings that provide more obstructions in propagating paths. However, studies at all three bands show that a majority of links can be made for T-R separation distances less than 200 m.

The first 3-D measurement-based mmWave wideband statistical channel impulse response model and key parameters were presented for 28 GHz propagation. Indoor and small-scale outdoor measurements are currently under way for the 28 and 73 GHz bands to build a larger database of mmWave measurements and to generate more diverse models. The data and models presented in this article will allow for the development of channel models and system analysis for next-generation mmWave small cell wireless communications systems, and may assist in the global comparison of models from other researchers.

## REFERENCES

- [1] T. S. Rappaport, R. W. Heath, Jr., R. C. Daniels, and J. N. Murdock, *Millimeter Wave Wireless Communications*. Englewood Cliffs, NJ, USA: Prentice Hall, 2015.
- [2] Z. Pi and F. Khan, “An introduction to millimeter-wave mobile broadband systems,” *IEEE Commun. Mag.*, vol. 49, no. 6, pp. 101–107, Jun. 2011.
- [3] T. S. Rappaport *et al.*, “Millimeter wave mobile communications for 5G cellular: It will work!” *IEEE Access*, vol. 1, pp. 335–349, May 2013.
- [4] F. Gutierrez, S. Agarwal, K. Parrish, and T. S. Rappaport, “On-chip integrated antenna structures in CMOS for 60 GHz WPAN systems,” *IEEE J. Sel. Areas Commun.*, vol. 27, no. 8, pp. 1367–1378, Oct. 2009.
- [5] T. S. Rappaport, J. N. Murdock, and F. Gutierrez, “State of the art in 60-GHz integrated circuits and systems for wireless communications,” in *Proc. IEEE*, vol. 99, no. 8, pp. 1390–1436, Aug. 2011.
- [6] T. S. Rappaport, W. Roh, and K. Cheun, “Mobile’s millimeter-wave makeover,” in *Proc. IEEE Spectr.*, vol. 51, no. 9, pp. 34–58, Sep. 2014.
- [7] T. S. Rappaport, “Keynote Speech: Millimeter Wave Wireless Communications—The Renaissance of Computing and Communications,” presented at the IEEE International Conference on Communications (ICC), Sydney, Australia, Jun. 2014, slides available at ICC 14 website.
- [8] “VNI mobile forecast highlights, 2014–2019,” CISCO, San Jose, CA, USA, 2015. [Online]. Available: [http://www.cisco.com/assets/sol/sp/vni/forecast\\_highlights\\_mobile/index.html](http://www.cisco.com/assets/sol/sp/vni/forecast_highlights_mobile/index.html)
- [9] “Cisco visual networking index: Mobile data traffic forecast update, 2013–2018,” CISCO, San Jose, CA, USA, Feb. 2014. [Online]. Available: [http://www.cisco.com/c/en/us/solutions/collateral/service-provider/visual-networking-index-vni/white\\_paper\\_c11-520862.pdf](http://www.cisco.com/c/en/us/solutions/collateral/service-provider/visual-networking-index-vni/white_paper_c11-520862.pdf)
- [10] “FutureWorks NSN White Paper: Looking ahead to 5G,” Nokia Solutions and Networks, Zoetermeer, The Netherlands, Dec. 2013. [Online]. Available: <http://networks.nokia.com/file/28771/5g-white-paper>
- [11] S. Y. Seidel and H. W. Arnold, “Propagation measurements at 28 GHz to investigate the performance of local multipoint distribution service (LMDS),” in *Proc. IEEE GLOBECOM*, Nov. 1995, vol. 1, pp. 754–757.
- [12] T. Pratt and C. W. Bostian, *Satellite Communications*. New York, NY, USA: Wiley, 1986.

- [13] Y. Azar *et al.*, "28 GHz propagation measurements for outdoor cellular communications using steerable beam antennas in New York City," in *Proc. IEEE ICC*, Jun. 2013, pp. 5143–5147.
- [14] G. R. MacCartney, Jr., J. Zhang, S. Nie, and T. S. Rappaport, "Path loss models for 5G millimeter wave propagation channels in urban microcells," in *Proc. IEEE GLOBECOM*, Dec. 2013, pp. 3948–3953.
- [15] "Before the federal communications commission," Federal Communications Commission, Washington, DC, USA, FCC 14-154, Oct. 2014. [Online]. Available: [https://apps.fcc.gov/edocs\\_public/attachmatch/FCC-14-154A1.pdf](https://apps.fcc.gov/edocs_public/attachmatch/FCC-14-154A1.pdf)
- [16] Federal Communications Commission, Washington, DC, USA, "FCC 14-177," Jan. 2015. [Online]. Available: <http://apps.fcc.gov/ecfs/proceeding/view?name=14-177>
- [17] "Spectrum above 6 GHz for future mobile communications," Ofcom, London, U.K., Feb. 2015. [Online]. Available: [http://stakeholders.ofcom.org.uk/binaries/consultations/above-6ghz/summary/spectrum\\_above\\_6\\_GHz\\_CFI.pdf](http://stakeholders.ofcom.org.uk/binaries/consultations/above-6ghz/summary/spectrum_above_6_GHz_CFI.pdf)
- [18] M. Kyro, V. Kolmonen, and P. Vainikainen, "Experimental propagation channel characterization of mm-wave radio links in urban scenarios," *IEEE Antennas Wireless Propag. Lett.*, vol. 11, pp. 865–868, Jul. 2012.
- [19] J. C. Liberti and T. S. Rappaport, "A geometrically based model for line-of-sight multipath radio channels," in *Proc. IEEE 46th Veh. Technol. Conf., Mobile Technol. Human Race*, Apr. 1996, vol. 2, pp. 844–848.
- [20] P. Petrus, J. H. Reed, and T. S. Rappaport, "Geometrical-based statistical macrocell channel model for mobile environments," *IEEE Trans. Commun.*, vol. 50, no. 3, pp. 495–502, Mar. 2002.
- [21] P. Petrus, J. H. Reed, and T. S. Rappaport, "Geometrically based statistical channel model for macrocellular mobile environments," in *Proc. IEEE GLOBECOM. Commun.: Key Global Prosperity*, Nov. 1996, vol. 2, pp. 1197–1201.
- [22] M. Kyro, S. Ranvier, V. Kolmonen, K. Haneda, and P. Vainikainen, "Long range wideband channel measurements at 81-86 GHz frequency range," in *Proc. 4th EuCAP*, Apr. 2010, pp. 1–5.
- [23] A. Elrefaie and M. Shakouri, "Propagation measurements at 28 GHz for coverage evaluation of local multipoint distribution service," in *Proc. Wireless Commun. Conf.*, Aug. 1997, pp. 12–17.
- [24] E. Violette, R. Espeland, R. DeBolt, and F. Schwering, "Millimeter-wave propagation at street level in an urban environment," *IEEE Trans. Geosci. Remote Sens.*, vol. 26, no. 3, pp. 368–380, May 1988.
- [25] F. Wang and K. Sarabandi, "An enhanced millimeter-wave foliage propagation model," *IEEE Trans. Antennas Propag.*, vol. 53, no. 7, pp. 2138–2145, Jul. 2005.
- [26] F. K. Schwering, E. J. Violette, and R. H. Espeland, "Millimeter-wave propagation in vegetation: Experiments and theory," *IEEE Trans. Geosci. Remote Sens.*, vol. 26, no. 3, pp. 355–367, May 1988.
- [27] C. Hansen, "WiGiG: Multi-gigabit wireless communications in the 60 GHz band," *IEEE Wireless Commun.*, vol. 18, no. 6, pp. 6–7, Dec. 2011.
- [28] G. Lovnes, J. Reis, and R. Raekken, "Channel sounding measurements at 59 GHz in city streets," in *Proc. 5th IEEE Int. Symp. Pers., Indoor Mobile Radio Commun. Wireless Netw.—Catching Mobile Future*, Sep. 1994, vol. 2, pp. 496–500.
- [29] P. F. M. Smulders and L. M. Correia, "Characterisation of propagation in 60 GHz radio channels," *Electron. Commun. Eng. J.*, vol. 9, no. 2, pp. 73–80, Apr. 1997.
- [30] T. S. Rappaport, *Wireless Communications: Principles and Practice*, 2nd ed. Upper Saddle River, NJ, USA: Prentice-Hall, 2002.
- [31] H. Thomas, R. Cole, and G. Siqueira, "An experimental study of the propagation of 55 GHz millimeter waves in an urban mobile radio environment," *IEEE Trans. Veh. Technol.*, vol. 43, no. 1, pp. 140–146, Feb. 1994.
- [32] W. Keusgen, R. Weiler, M. Peter, M. Wisotzki, and B. Goktepe, "Propagation measurements and simulations for millimeter-wave mobile access in a busy urban environment," in *Proc. 39th IRMMW-THz*, Sep. 2014, pp. 1–3.
- [33] S. Rajagopal, S. Abu-Surra, and M. Malmirchegini, "Channel feasibility for outdoor non-line-of-sight mmwave mobile communication," in *Proc. IEEE VTC—Fall*, Sep. 2012, pp. 1–6.
- [34] T. S. Rappaport, E. Ben-Dor, J. N. Murdock, and Y. Qiao, "38 GHz and 60 GHz angle-dependent propagation for cellular and peer-to-peer wireless communications," in *Proc. IEEE ICC*, Jun. 2012, pp. 4568–4573.
- [35] T. S. Rappaport, F. Gutierrez, Jr., E. Ben-Dor, J. N. Murdock, Y. Qiao, and J. I. Tamir, "Broadband millimeter-wave propagation measurements and models using adaptive-beam antennas for outdoor urban cellular communications," in *IEEE Trans. Antennas Propag.*, vol. 61, no. 4, pp. 1850–1859, Apr. 2013.
- [36] T. S. Rappaport, Y. Qiao, J. I. Tamir, J. N. Murdock, and E. Ben-Dor, "Cellular broadband millimeter wave propagation and angle of arrival for adaptive beam steering systems (invited paper)," in *Proc. IEEE RWS*, Jan. 2012, pp. 151–154.
- [37] T. S. Rappaport, W. Roh, and K. Cheun, "Mobile's millimeter-wave makeover," *IEEE Spectrum*, vol. 51, no. 9, pp. 34–58, Sept. 2014.
- [38] G. R. MacCartney, Jr., M. K. Samimi, and T. S. Rappaport, "Omnidirectional path loss models in New York City at 28 GHz and 73 GHz," in *Proc. IEEE 25th Int. Symp. PIMRC*, Sep. 2014.
- [39] M. R. Akdeniz *et al.*, "Millimeter wave channel modeling and cellular capacity evaluation," *IEEE J. Sel. Areas Commun.*, vol. 32, no. 6, pp. 1164–1179, Jun. 2014.
- [40] S. Rangan, T. S. Rappaport, and E. Erkip, "Millimeter-wave cellular wireless networks: Potentials and challenges," in *Proc. IEEE*, vol. 102, no. 3, pp. 366–385, Mar. 2014.
- [41] G. R. MacCartney, Jr., M. K. Samimi, and T. S. Rappaport, "Exploiting directionality for millimeter-wave wireless system improvement," in *Proc. IEEE ICC*, Jun. 2015, pp. 1–7.
- [42] S. Hur *et al.*, "Synchronous channel sounder using horn antenna and indoor measurements on 28 GHz," in *Proc. IEEE Int. BlackSeaCom*, May 2014, pp. 83–87.
- [43] W. Roh *et al.*, "Millimeter-wave beamforming as an enabling technology for 5G cellular communications: Theoretical feasibility and prototype results," *IEEE Commun. Mag.*, vol. 52, no. 2, pp. 106–113, Feb. 2014.
- [44] S. Sun, G. R. MacCartney, Jr., M. K. Samimi, S. Nie, and T. S. Rappaport, "Millimeter wave multi-beam antenna combining for 5G cellular link improvement in New York City," in *Proc. IEEE ICC*, Jun. 2014, pp. 5468–5473.
- [45] M. K. Samimi and T. S. Rappaport, "Ultra-wideband statistical channel model for non line of sight millimeter-wave urban channels," in *Proc. IEEE GLOBECOM*, Dec. 2014, pp. 3483–3489.
- [46] M. K. Samimi and T. S. Rappaport, "3-D statistical channel model for millimeter-wave outdoor mobile broadband communications," in *Proc. IEEE ICC*, Jun. 2015, pp. 1–7.
- [47] S. Deng, C. J. Slezak, G. R. MacCartney, Jr., and T. S. Rappaport, "Small wavelengths—Big potential: millimeter wave propagation measurements for 5G," *Microw. J.*, vol. 57, no. 11, pp. 4–12, Sep. 2014.
- [48] A. I. Sulyman *et al.*, "Radio propagation path loss models for 5G cellular networks in the 28 GHz and 38 GHz millimeter-wave bands," *IEEE Commun. Mag.*, vol. 52, no. 9, pp. 78–86, Sep. 2014.
- [49] S. Sun, T. S. Rappaport, R. W. Heath, A. Nix, and S. Rangan, "Mimo for millimeter-wave wireless communications: beamforming, spatial multiplexing, or both?" *IEEE Commun. Mag.*, vol. 52, no. 12, pp. 110–121, Dec. 2014.
- [50] "Spatial channel model for multiple input multiple output (MIMO) simulations," 3rd Generation Partnership Project, Sophia Antipolis Cedex, France, TR 25.996, Sep. 2003. [Online]. Available: <http://www.3gpp.org>
- [51] S. C. Swales, T. Busby, D. J. Purle, M. A. Beach, and J. P. McGeehan, "A comparison of CDMA techniques for third generation mobile radio systems," in *Proc. 43rd IEEE Veh. Technol. Conf.*, May 1993, pp. 424–427.
- [52] J. C. Liberti and T. S. Rappaport, "Analysis of CDMA cellular radio systems employing adaptive antennas in multipath environments," in *Proc. IEEE 46th Veh. Technol. Conf. Mobile Technol. Human Race.*, Apr. 1996, vol. 2, pp. 1076–1080.
- [53] G. Durgin, N. Patwari, and T. Rappaport, "An advanced 3D ray launching method for wireless propagation prediction," in *Proc. IEEE 47th Veh. Technol. Conf.*, May 1997, vol. 2, pp. 785–789.
- [54] B. D. Woerner, J. H. Reed, and T. S. Rappaport, "Simulation issues for future wireless modems," *IEEE Commun. Mag.*, vol. 32, no. 7, pp. 42–53, Jul. 1994.
- [55] Z. Rong, T. S. Rappaport, P. Petrus, and J. H. Reed, "Simulation of multitarget adaptive array algorithms for wireless CDMA systems," in *Proc. IEEE 47th Veh. Technol. Conf.*, May 1997, vol. 1, pp. 1–5.
- [56] N. C. Barati *et al.*, "Directional cell discovery in millimeter wave cellular networks," *IEEE Trans. Wireless Communications*, to be published.
- [57] F. Gutierrez, Jr., T. S. Rappaport, and J. Murdock, "Millimeter-wave CMOS antennas and RFIC parameter extraction for vehicular applications," in *Proc. IEEE 72nd VTC—Fall*, Sep. 2010, pp. 1–6.
- [58] K. Hassan, T. S. Rappaport, and J. G. Andrews, "Analog equalization for low power 60 GHz receivers in realistic multipath channels," in *Proc. IEEE GLOBECOM*, Dec. 2010, pp. 1–5.
- [59] A. Ghosh *et al.*, "Millimeter-wave enhanced local area systems: A high-data-rate approach for future wireless networks," *IEEE J. Sel. Areas Commun.*, vol. 32, no. 6, pp. 1152–1163, Jun. 2014.

- [60] A. Adhikary *et al.*, "Joint spatial division and multiplexing for mm-wave channels," *IEEE J. Sel. Areas Commun.*, vol. 32, no. 6, pp. 1239–1255, Jun. 2014.
- [61] E. Ben-Dor, T. S. Rappaport, Y. Qiao, and S. J. Lauffenburger, "Millimeter-wave 60 GHz outdoor and vehicle AOA propagation measurements using a broadband channel sounder," in *Proc. IEEE GLOBECOM*, Dec. 2011, pp. 1–6.
- [62] M. K. Samimi *et al.*, "28 GHz angle of arrival and angle of departure analysis for outdoor cellular communications using steerable beam antennas in New York City," in *Proc. IEEE 77th VTC—Spring*, Jun. 2013, pp. 1–6.
- [63] S. Nie, G. R. MacCartney, Jr., S. Sun, and T. S. Rappaport, "72 GHz millimeter wave indoor measurements for wireless and backhaul communications," in *Proc. IEEE 24th Int. Symp. PIMRC*, Sep. 2013, pp. 2429–2433.
- [64] S. Sun and T. S. Rappaport, "Multi-beam antenna combining for 28 GHz cellular link improvement in urban environments," in *Proc. IEEE GLOBECOM*, Dec. 2013, pp. 3754–3759.
- [65] G. R. MacCartney, Jr. and T. S. Rappaport, "73 GHz millimeter wave propagation measurements for outdoor urban mobile and backhaul communications in New York City," in *Proc. IEEE ICC*, Jun. 2014, pp. 4862–4867.
- [66] WP5: Propagation, antennas and multi-antenna technique, channel modeling and characterization," in *Proc. MiWEBA Deliverable D5.1*, Jun. 2014, pp. 12–14.
- [67] D. Cox, "Delay Doppler characteristics of multipath propagation at 910 MHz in a suburban mobile radio environment," *IEEE Trans. Antennas Propag.*, vol. 20, no. 5, pp. 625–635, Sep. 1972.
- [68] G. Martin, "Wideband channel sounding dynamic range using a sliding correlator," in *Proc. IEEE 51st VTC—Spring*, Tokyo, Japan, 2000, vol. 3, pp. 2517–2521.
- [69] R. J. Pirkl and G. D. Durgin, "Optimal sliding correlator channel sounder design," *IEEE Trans. Wireless Commun.*, vol. 7, no. 9, pp. 3488–3497, Sep. 2008.
- [70] W. G. Newhall, T. S. Rappaport, and D. G. Sweeney, "A spread spectrum sliding correlator system for propagation measurements," in *Proc. RF Design*, pp. 40–54, Apr. 1996.
- [71] A. Bottcher, C. Schneider, P. Vary, and R. S. Thoma, "Dependency of the power and delay domain parameters on antenna height and distance in urban macro cell," in *Proc. 5th EUCAP*, Apr. 2011, pp. 1395–1399.
- [72] S. Sun and T. Rappaport, "Wideband mmwave channels: Implications for design and implementation of adaptive beam antennas," in *Proc. IEEE MTT-S IMS*, Jun. 2014, pp. 1–4.
- [73] "NYU WIRELESS mmWave Propagation Database," NYU WIRELESS, Brooklyn, NY, USA.
- [74] T. S. Rappaport, S. DiPierro, and R. Akturan, "Analysis and simulation of interference to vehicle-equipped digital receivers from cellular mobile terminals operating in adjacent frequencies," *IEEE Trans. Veh. Technol.*, vol. 60, no. 4, pp. 1664–1676, May 2011.
- [75] H. C. Nguyen *et al.*, "Evaluation of empirical ray-tracing model for an urban outdoor scenario at 73 GHz e-band," in *Proc. IEEE 80th VTC—Fall*, Sep. 2014, pp. 1–6.
- [76] P. Kyosti *et al.*, "WINNER II channel models," Eur. Commission, Brussels, Belgium, IST-WINNER, Tech. Rep. D1.1.2.
- [77] M. Hata, "Empirical formula for propagation loss in land mobile radio services," *IEEE Trans. Veh. Technol.*, vol. 29, no. 3, pp. 317–325, Aug. 1980.
- [78] F. Gutierrez, K. Parrish, and T. S. Rappaport, "On-chip integrated antenna structures in CMOS for 60 GHz WPAN systems," in *Proc. IEEE GLOBECOM*, Nov. 2009, pp. 1–7.
- [79] M. Feuerstein, K. Blackard, T. Rappaport, S. Seidel, and H. Xia, "Path loss, delay spread, and outage models as functions of antenna height for microcellular system design," *IEEE Trans. Veh. Technol.*, vol. 43, no. 3, pp. 487–498, Aug. 1994.
- [80] J. N. Murdock, E. Ben-Dor, Y. Qiao, J. I. Tamir, and T. S. Rappaport, "A 38 GHz cellular outage study for an urban outdoor campus environment," in *Proc. IEEE WCNC*, Apr. 2012, pp. 3085–3090.
- [81] P. B. Papazian, M. Roadifer, and G. A. Hufford, "Initial study of the local multipoint distribution system radio channel," Nat. Telecommun. Inf. Admin., Boulder, CO, USA, NTIA Report 94-315, Aug. 1994.
- [82] S. Nie, G. R. MacCartney, S. Sun, and T. S. Rappaport, "28 GHz and 73 GHz signal outage study for millimeter wave cellular and backhaul communications," in *Proc. IEEE ICC*, Jun. 2014, pp. 4856–4861.
- [83] "Further advancements for e-utra physical layer aspects (release 9)," 3rd Generation Partnership Project, Sophia Antipolis Cedex, France, 3GPP TR 36.814, Mar. 2010. [Online]. Available: <http://www.3gpp.org/DynaReport/36814.htm>
- [84] T. Bai and R. W. Heath, Jr., "Coverage and rate analysis for millimeter-wave cellular networks," *IEEE Trans. Wireless Commun.*, vol. 14, no. 2, pp. 1100–1114, Feb. 2015.
- [85] A. Molisch, "Statistical properties of the RMS delay-spread of mobile radio channels with independent rayleigh-fading paths," *IEEE Trans. Veh. Technol.*, vol. 45, no. 1, pp. 201–204, Feb. 1996.
- [86] Q. Spencer, M. Rice, B. Jeffs, and M. Jensen, "A statistical model for angle of arrival in indoor multipath propagation," in *Proc. IEEE 47th VTC*, May 1997, vol. 3, pp. 1415–1419.
- [87] A. A. M. Saleh and R. A. Valenzuela, "A statistical model for indoor multipath propagation," *IEEE J. Sel. Areas Commun.*, vol. 5, no. 2, pp. 128–137, Feb. 1987.
- [88] T. A. Thomas, H. C. Nguyen, G. R. MacCartney, Jr., and T. S. Rappaport, "3D mmWave channel model proposal," in *Proc. IEEE 80th VTC—Fall*, Sep. 2014, pp. 1–6.
- [89] R. B. Ertel, P. Cardieri, K. W. Sowerby, T. S. Rappaport, and J. H. Reed, "Overview of spatial channel models for antenna array communication systems," *IEEE Pers. Commun.*, vol. 5, no. 1, pp. 10–22, Feb. 1998.
- [90] J. S. Bendat and A. G. Piersol, *Random Data: Analysis and Measurement Procedures*. Wiley, 2010.
- [91] T. S. Rappaport and S. Deng, "73 GHz wideband millimeter-wave foliage and ground reflection measurements and models," in *Proc. IEEE ICC Workshops*, Jun. 2015.
- [92] H. Zhao, *et al.*, "28 GHz millimeter wave cellular communication measurements for reflection and penetration loss in and around buildings in New York city," in *Proc. IEEE ICC*, Jun. 2013, pp. 5163–5167.
- [93] M. K. Samimi, T. S. Rappaport, and G. R. MacCartney, Jr., "Probabilistic omnidirectional path loss models for millimeter-wave outdoor communications," *IEEE Wireless Commun. Lett.*, Mar. 2015.
- [94] G. R. MacCartney, T. S. Rappaport, M. K. Samimi, and S. Sun, "Millimeter wave omnidirectional path loss data for small cell 5G channel modeling," *IEEE Access*, to be published.



**Theodore S. Rappaport** (S'83–M'84–SM'91–F'98) is the David Lee/Ernst Weber Professor of Electrical and Computer Engineering with New York University (NYU) Polytechnic School of Engineering, Brooklyn, NY, USA, and is the Founding Director of NYU WIRELESS. He also holds professorship positions with Courant Institute of Mathematical Sciences and the School of Medicine, NYU. He founded major wireless research centers at Virginia Polytechnic Institute and State University (MPRG), The University of Texas at Austin (WNCG), and NYU (NYU WIRELESS), and founded two wireless technology companies that were sold to publicly traded firms. He is a highly sought-after technical consultant having testified before the U.S. Congress and having served the ITU. He has advised more than 100 students, has more than 100 patents issued and pending, and has authored or coauthored several books, including the best-seller *Wireless Communications: Principles and Practice* (2nd ed., Prentice Hall, 2002). His latest book, *Millimeter Wave Wireless Communications* (Pearson/Prentice Hall ©2015), is the first comprehensive text on the subject.



**George R. MacCartney, Jr.** (S'08) received the B.S. and M.S. degrees in electrical engineering from Villanova University, Villanova, PA, USA, in 2010 and 2011, respectively. He is currently working toward the Ph.D. degree in electrical engineering with New York University, Polytechnic School of Engineering, Brooklyn, NY, USA, under the supervision of Prof. Rappaport in the NYU WIRELESS Research Center. He has authored or co-authored more than ten technical papers in the field of mmWave propagation, and his research interests include mmWave propagation test and measurement prototyping, and channel modeling and analysis for 5G communications.



**Mathew K. Samimi** (S'13) received the B.S. degree in applied physics from the Fu Foundation School of Engineering and Applied Science of Columbia University, New York, NY, USA, in 2012 and the M.S. degree in electrical engineering from the NYU Polytechnic School of Engineering, Brooklyn, NY, in 2014. He is currently working toward the Ph.D. degree in electrical engineering at the NYU WIRELESS Research Center, Department of Electrical and Computer Engineering, NYU Polytechnic School of Engineering, under the supervision of Prof. Rappaport,

and is developing millimeter-wave statistical spatial channel models for next-generation ultrawideband mobile cellular in dense urban environments.



**Shu Sun** (S'13) received the B.S. degree in applied physics from Shanghai Jiao Tong University, China, in 2012. She is currently working toward the Ph.D. degree in electrical engineering at Polytechnic School of Engineering, New York University (NYU), Brooklyn, and is doing research at the NYU WIRELESS Research Center. She has authored or co-authored more than ten technical papers in the field of wireless communications. Her current research interests include millimeter-wave (mmWave) mobile communications and the analysis of MIMO systems

for mmWave channels.